Inorg. Chem. **2005**, *44*, 779–797

Forum

Paramagnetic NMR Spectroscopy and Density Functional Calculations in the Analysis of the Geometric and Electronic Structures of Iron–Sulfur Proteins

Timothy E. Machonkin

Department of Biochemistry and Biophysics, University of Rochester, 601 Elmwood Drive, Box #712, Rochester, New York 14642

William M. Westler and John L. Markley*

Department of Biochemistry and Nuclear Magnetic Resonance Facility at Madison, University of Wisconsin, 433 Babcock Drive, Madison, Wisconsin 53706

Received October 1, 2004

Paramagnetic NMR spectroscopy has been underutilized in the study of metalloproteins. One difficulty of the technique is that paramagnetic relaxation broadens signals from nuclei near paramagnetic centers. In systems with low electronic relaxation rates, this makes such signals difficult to observe or impossible to assign by traditional methods. We show how the challenges of detecting and assigning signals from nuclei near the metal center can be overcome through the combination of uniform and selective ^{2}H, ^{13}C, and ^{15}N isotopic labeling with NMR experiments that utilize direct one-dimensional (^{2}H, ^{13}C, and ^{15}N) and two-dimensional (^{13}C–X) detection. We have developed methods for calculating NMR chemical shifts and relaxation rates by density functional theory (DFT) approaches. We use the correspondence between experimental NMR parameters and those calculated from structural models of iron–sulfur clusters derived from X-ray crystallography to validate the computational approach and to investigate how structural differences are manifested in these values. We have applied this strategy to three iron–sulfur proteins: *Clostridium pasteurianum* rubredoxin, *Anabaena* [2Fe–2S] ferredoxin, and human [2Fe–2S] ferredoxin. Provided that an accurate structural model of the iron–sulfur cluster and surrounding residues is available from diffraction data, our results show that DFT calculations can return NMR observables with excellent accuracy. This suggests that it might be possible to use calculations to refine structures or to generate structural models of active sites when crystal structures are unavailable. The approach has yielded insights into the electronic structures of these iron–sulfur proteins. In rubredoxin, the results show that substantial unpaired electron spin is delocalized across NH···S hydrogen bonds and that the reduction potential can be changed by 77 mV simply by altering the strength of one of these hydrogen bonds. In reduced [2Fe–2S] ferredoxins, hyperfine shift data have provided quantitative information on the degree of valence trapping. The approach described here for iron–sulfur proteins offers new avenues for detailed studies of these and other metalloprotein systems.

1. Introduction

NMR spectroscopy has proven to be a powerful tool in the study of paramagnetic proteins.[1−9] NMR spectroscopy has frequently been used to obtain solution structures of certain classes of metalloproteins, most notably heme and [4Fe−4S] proteins, in which pseudocontact shifts can be used as structural constraints. However, paramagnetic NMR spectroscopy is an ideal tool for the study of the geometry and electronic structure of metalloprotein active sites as well.

Optical spectroscopies (absorption, circular dichroism, and magnetic circular dichroism), resonance Raman spectroscopy, X-ray absorption spectroscopies, Mössbauer spectroscopy

* To whom correspondence should be addressed. Tel.: (608)-263-9349. E-mail: markley@nmrfam.wisc.edu.

(1) Bertini, I.; Luchinat, C. *NMR of Paramagnetic Molecules in Biological System*; Benjamin/Cummings: Menlo Park, CA, 1986.

10.1021/ic048624j CCC: $30.25
Published on Web 01/29/2005

(for Fe-containing systems), and electron paramagnetic resonance (EPR) spectroscopy are all well-established methods in metalloprotein chemistry for the study of the electronic structure and coordination geometry of metal centers. When ligands or other moieties more distant from the metal center are the focus of study, then EPR-based techniques such as electron−nuclear double resonance (ENDOR) and electron spin−echo envelope modulation (ESEEM) spectroscopies have been the methods of choice. Many of the same electron−nuclear interactions manifested in ENDOR spectra also appear in NMR spectra of paramagnetic systems (paramagnetic NMR spectroscopy). Paramagnetic NMR spectroscopy can offer several potential advantages over the ENDOR and ESEEM techniques: (1) superior resolution of signals, (2) unambiguous assignments of signals, (3) applicability to $S > {}^1/_2$ systems, and (3) little or no requirement for specialized hardware (given that NMR spectrometers are so widely available). Traditionally, the major limitations have been that (1) paramagnetic NMR spectroscopy was restricted to systems with high electronic relaxation rates and therefore modest line broadening due to paramagnetic relaxation and (2) quantitative interpretation of hyperfine shifts and paramagnetic relaxation rates was often difficult. These limitations are now disappearing, because of the development of newer NMR methodologies, combined with the ability to perform quantum chemical calculations on sufficiently large models of metalloprotein active sites. This Forum article focuses on the application of some of these newer approaches in NMR spectroscopy and the use of quantum chemical calculations to study the active sites of a few iron−sulfur proteins. We begin with a brief review of the theory behind paramagnetic NMR spectroscopy; we then describe the NMR techniques, isotopic labeling strategies, and computational approaches we and others have developed; finally, we show how these approaches have been applied in studies of several iron−sulfur proteins.

2. Theory of Paramagnetic NMR Spectroscopy

Interactions between the unpaired electron spin on a metal center and the nuclear spins of surrounding atoms can give rise to several different observable NMR phenomena: hyperfine shifts,[8,10] paramagnetic relaxation,[8,11] residual dipolar couplings by magnetic alignment,[12−15] and cross-correlated relaxation.[16−21] We focus here on hyperfine shifts and paramagnetic relaxation, the two most readily observable paramagnetic phenomena in NMR spectroscopy.

2.1. Hyperfine Shifts. The chemical shifts observed in a paramagnetic system are the sum of the diamagnetic chemical shift, δ_{dia}, and the paramagnetic contribution, called the hyperfine shift. This can result in resonances appearing far outside the region typical for diamagnetic shifts. Hyperfine shifts, in turn, have two major contributions: the Fermi contact shift, δ_{con}, and the electron−nuclear dipolar or pseudocontact shift, δ_{pc}. The observed chemical shift, δ_{tot}, is the sum of all three

$$\delta_{tot} = \delta_{con} + \delta_{pc} + \delta_{dia} \tag{1}$$

The Fermi contact shift arises from the delocalization of unpaired electron spin density into ligand orbitals (a "through-bond" effect). Only unpaired spin density at the nucleus contributes to the Fermi contact coupling. The equation for the Fermi contact shift in parts per million is[10]

$$\delta_{con} = 10^6\left(\frac{\Delta\nu}{\nu_0}\right)^{con} = -10^6\frac{A}{\hbar\gamma_N B_0}\langle S_z\rangle \tag{2}$$

where A is the isotropic hyperfine constant in joules and $\langle S_z\rangle$ is the expectation value of S_z. Hyperfine coupling is frequently reported as A/h, which has units of hertz. In the absence of first-order orbital angular momentum or zero-field splitting (ZFS), this simplifies to

$$\delta_{con} = 10^6\left(\frac{\Delta\nu}{\nu_0}\right)^{con} = 10^6\left(\frac{A}{\hbar}\right)\frac{g\mu_B S(S+1)}{3\gamma_N kT} \tag{3}$$

where g is the average molecular electron g value (often assumed to be $\sim g_e$, the free-electron g value). Note that for high-spin (hs) Fe(III), this approximation introduces no real errors, as the ZFS is very small. For hs Fe(II), this approximation might not hold as well, especially for six-coordinate systems with unquenched orbital angular momentum. The isotropic hyperfine coupling constant, in turn, can be related to the unpaired spin density at the nucleus

$$A = \frac{\mu_0}{3S}\hbar\gamma_N g\mu_B\sum_i[|\psi_i^-(0)|^2 - |\psi_i^+(0)|^2] \tag{4}$$

where $|\psi_i^-(0)|^2$ and $|\psi_i^+(0)|^2$ are the negative and positive spin densities, respectively, at the nucleus of the ith molecular orbital. Fermi contact shifts in NMR spectroscopy are

(2) Bertini, I.; Turano, P.; Vila, A. J. *Chem. Rev.* **1993**, *93*, 2833−2932.
(3) Cheng, H.; Markley, J. L. *Annu. Rev. Biophys. Biomol. Struct.* **1995**, *24*, 209−237.
(4) Bertini, I.; Luchinat, C.; Rosato, A. *Prog. Biophys. Mol. Biol.* **1996**, *66*, 43−80.
(5) Bertini, I.; Luchinat, C.; Rosato, A. *Adv. Inorg. Chem.* **1999**, *47*, 251−282.
(6) Goodfellow, B. J.; Macedo, A. L. *Annu. Rep. NMR Spectrosc.* **1999**, *37*, 119−177.
(7) Bertini, I.; Luchinat, C.; Piccioli, M. *Methods Enzymol.* **2001**, *339*, 314−340.
(8) Bertini, I.; Luchinat, C.; Parigi, G. *Solution NMR of Paramagnetic Molecules*; Elsevier: Amsterdam, 2001.
(9) Machonkin, T. E.; Markley, J. L. In *Encyclopedia of Nuclear Magnetic Resonance*; Grant, D. M., Harris, R. K., Ed.; Wiley: Chichester, U.K., 2002; Vol. 9, pp 384−401.
(10) Kurland, R. J.; McGarvey, B. R. *J. Magn. Reson.* **1970**, *2*, 286−301.
(11) Banci, L.; Bertini, I.; Luchinat, C. *Nuclear and Electron Relaxation*; VCH: Weinheim, Germany, 1991.
(12) Bothner-By, A. A.; Domaille, P. J.; Gayathri, C. *J. Am. Chem. Soc.* **1981**, *103*, 5602−5603.
(13) Tolman, J. R.; Flanagan, J. M.; Kennedy, M. A.; Prestegard, J. H. *Proc. Natl. Acad. Sci. U.S.A.* **1995**, *92*, 9279−9283.
(14) Banci, L.; Bertini, I.; Huber, J. G.; Luchinat, C.; Rosato, A. *J. Am. Chem. Soc.* **1998**, *120*, 12903−12909.
(15) Volkman, B. F.; Wilkens, S. J.; Lee, A. L.; Xia, B.; Westler, W. W.; Berger, R.; Markley, J. L. *J. Am. Chem. Soc.* **1999**, *120*, 4677−4683.
(16) Werbelow, L.; Thevand, A. *J. Magn. Reson. A* **1993**, *101*, 317−319.
(17) Kumar, A.; Madhu, P. K. *Concepts Magn. Reson.* **1996**, *8*, 139−160.
(18) Desvaux, H.; Gochin, M. *Mol. Phys.* **1999**, *96*, 1317−1333.
(19) Boisbouvier, J.; Gans, P.; Blackledge, M.; Brutscher, B.; Marion, D. *J. Am. Chem. Soc.* **1999**, *121*, 7700−7701.
(20) Mandal, P. K.; Madhu, P. K.; Müller, N. *Chem. Phys. Lett.* **2000**, *320*, 269−276.
(21) Madhu, P. K.; Grandori, R.; Hohenthanner, K.; Mandal, P. K.; Müller, N. *J. Biomol. NMR* **2001**, *20*, 31−37.

exquisitely sensitive to even very small amounts of unpaired electron spin density, and the only upper limit to the magnitude of Fermi contact couplings that can be observed is a practical limitation of detecting lines that are excessively broadened by paramagnetic relaxation (vide infra).

The second contribution to the hyperfine shift arises from the dipolar coupling of the unpaired electron spin with the nuclear spins of surrounding atoms (i.e., a "through-space" effect). The magnetic moment of the electron is *anisotropic* as a result of coupling between the spin and orbital angular momenta. Because the magnetic moment of the electron changes with orientation, the electron−nuclear dipolar coupling does not average to zero with molecular tumbling, but rather yields an *isotropic* shift that is dependent on both the electron−nuclear distance and the orientation of the electron−nucleus vector with respect to the magnetic susceptibility tensor. Although the unpaired electron spin is delocalized, the simplest approximation is to assume that the electron spin is localized at the metal center, the "point-dipole" approximation, yielding[10]

$$\delta_{pc} = 10^6\left(\frac{\Delta\nu}{\nu_0}\right)^{pc} = 10^6\frac{1}{8\pi r^3}\left[(3\cos^2\theta - 1)\left(\frac{2}{3}\chi_{zz} - \frac{1}{3}\chi_{xx} - \frac{1}{3}\chi_{yy}\right) + \sin^2\theta\cos 2\phi(\chi_{xx} - \chi_{yy})\right] \quad (5)$$

where r is the electron−nuclear distance; χ_{zz}, χ_{xx}, and χ_{yy} are the principal components of the magnetic susceptibility tensor; and θ and ϕ are the angles formed by r and the molecular z axis and the projection of r in the xy plane with the molecular x axis, respectively.

2.2. Paramagnetic Relaxation. The proximity of unpaired electron spin to a nuclear spin provides facile mechanisms for relaxation of the nuclear spin. This leads to large challenges in paramagnetic NMR spectroscopy, because severe line broadening can hinder the detection and resolution of resonances and can render useless most traditional multidimensional experiments. However, paramagnetic relaxation rates contain useful information, provided that they can be determined. The paramagnetic contributions to the familiar nuclear T_1 and T_2 relaxation times arise from several different contributions: electron−nuclear dipolar, contact, and Curie spin (which arises from the interaction between the nuclear spin and the large, time-averaged magnetic moment of the electron).[22,23] These paramagnetic effects can shorten nuclear T_1 and T_2 relaxation times by many orders of magnitude. The commonly encountered equations for dipolar and contact relaxation are the Solomon−Bloembergen−Morgan equations.[24,25] In these equations, several simplifying assumptions are again made: the point-dipole approximation holds, g is isotropic, and ZFS is negligible. For example, the dipolar contribution to T_1 is given by

$$T_{1_{dip}}^{-1} = \frac{2}{15}\left(\frac{\mu_0}{4\pi}\right)^2\frac{\gamma_N^2 g^2\mu_B^2 S(S+1)}{r^6}\left[\frac{\tau_c}{1+(\omega_I-\omega_S)^2\tau_c^2} + \frac{3\tau_c}{1+\omega_I^2\tau_c^2} + \frac{6\tau_c}{1+(\omega_I+\omega_S)^2\tau_c^2}\right] \quad (6)$$

where ω_I and ω_S are the nuclear and electron Larmor precession frequencies, respectively; τ_r is the rotational correlation time; τ_e is the electronic relaxation time; and τ_c is the total correlation time, given as

$$\tau_c^{-1} = \tau_r^{-1} + \tau_e^{-1} \quad (7)$$

One complication is the origin of τ_e. Electron spin has its own longitudinal and transverse relaxation times, T_{1e} and T_{2e}, that arise from a number of different mechanisms, which for room-temperature solutions of transition metals are complex and not entirely understood. Therefore, one frequently finds that the electronic relaxation time is given a single value, τ_e, that is empirically derived from fitting the Solomon−Bloembergen−Morgan equations to experimental data. For example, τ_e is typically $\sim 10^{-10}-10^{-11}$ s for mononuclear high-spin (hs) Fe^{3+} and $\sim 10^{-11}-10^{-12}$ s for mononuclear hs Fe^{2+}.[11] Several groups have derived more complex equations that seek to overcome the weaknesses of the Solomon−Bloembergen−Morgan equations.[8,11,26−29]

For macromolecules, the dominant paramagnetic contribution to T_1 is the electron−nuclear coupling, thus making T_1 values an excellent source of geometric information. For systems with high electronic relaxation rates and high-spin metal centers and/or high molecular masses, Curie spin relaxation can be the dominant contribution to T_2, especially at the high fields used in modern NMR spectroscopy. For systems with low electronic relaxation rates and with lower spin states (e.g., $S = {}^1/_2$) and/or modest molecular masses, contact relaxation can be the dominant contribution to T_2 for the most hyperfine-shifted resonances.

Although pseudocontact shifts and paramagnetic T_1 relaxation times can be powerful sources of geometric information for the region around a metal center, because both are strongly dependent on the distance between the nucleus and the unpaired electron spin and because pseudocontact shifts have an additional angular dependence, both suffer the problem that unpaired electron spin density is delocalized over many orbitals. Therefore, of all of the assumptions that go into the commonly employed equations for pseudocontact shifts and paramagnetic T_1 relaxation times (eqs 5 and 7), it is the point-dipole approximation that leads to the largest failure in a quantitative analysis of such data. This is especially notable for systems such as iron−sulfur proteins, in which the metal center is appreciably covalent and electron delocalization onto the ligands contributes significantly to the observed effects in paramagnetic NMR spectra. This is sometimes referred to as the "ligand-centered" contribution to the pseudocontact shift and dipolar relaxation time. One

(22) Gueron, M. *J. Magn. Reson.* **1975**, *19*, 58−66.
(23) Vega, A. J.; Fiat, D. *Mol. Phys.* **1976**, *31*, 347−355.
(24) Solomon, I. *Phys. Rev.* **1955**, *99*, 559−565.
(25) Bloembergen, N.; Morgan, L. O. *J. Chem. Phys.* **1961**, *34*, 842−850.
(26) Bertini, I.; Galas, O.; Luchinat, C.; Parigi, G. *J. Magn. Reson. A* **1995**, *113*, 151−158.
(27) Kowalewski, J.; Nordenskiöld, L.; Benetis, N.; Westlund, P.-O. *Prog. NMR Spectrosc.* **1985**, *17*, 141−185.
(28) Westlund, P.-O. In *Dynamics of Solutions and Fluid Mixtures by NMR*; Delpuech, J.-J., Ed.; John Wiley & Sons: Chichester, U.K., 1995; pp 173−229.
(29) Sharp, R.; Lohr, L.; Miller, J. *Prog. NMR Spectrosc.* **2001**, *38*, 115−158.

of the simplest and most accurate approaches for dealing with delocalized unpaired electron spin when calculating electron−nuclear dipolar relaxation rates is to replace the point-dipole electron−nuclear distance in eq 7, r, with an *effective* distance, r_{eff}. This effective distance can be calculated by describing the unpaired electron spin density as a density matrix.[30] Alternatively, r_{eff} can be rewritten in terms of the elements of the *spin-differential field gradient tensor*[31,32]

$$r_{eff}^{-6} = \frac{1}{4}\left[\frac{1}{3}(\langle q_{xx}\rangle_{spin} - \langle q_{yy}\rangle_{spin})^2 + \langle q_{zz}\rangle_{spin}^2 + \frac{4}{3}(\langle q_{xy}\rangle_{spin}^2 + \langle q_{xz}\rangle_{spin}^2 + \langle q_{yz}\rangle_{spin}^2)\right] \quad (8)$$

These matrix elements, $\langle q_{\alpha\beta}\rangle_{spin}$, are given by

$$\langle q_{\alpha\beta}\rangle_{spin} = \sum_{st} D_{st}\langle s|\hat{q}|t\rangle \quad (9)$$

where D_{st} is the normalized, spin-only density matrix and $q_{\alpha\beta}$ is the electric field gradient tensor operator (which has the same angular dependence as the magnetic dipole operator)

$$\hat{q}_{\alpha\beta} = (3r_\alpha r_\beta - \delta_{\alpha\beta}r^2)/r^5 \quad (10)$$

In this approach, the simplicity of the Solomon−Bloembergen−Morgan equation for T_1 (eq 7) is retained, but the impact that electron delocalization has on dipolar relaxation can be considered quantitatively by means that are readily calculable with modern quantum chemical methods (vide infra). A similar approach can be taken for the calculation of pseudocontact shifts.

2.3. Exchange Coupling and Its Influence on Electron−Nuclear Interactions. Exchange coupling between the unpaired electrons in binuclear and larger metal clusters has a significant impact on the properties observed by paramagnetic NMR spectroscopy. Here, we present the basic theory of exchange coupling and show how the vector coupling model can be used to describe the impact of exchange coupling on hyperfine shifts and relaxation rates.

In a coupled system, exchange coupling can be described by a phenomenological spin Hamiltonian[33]

$$\mathscr{H} = \sum_{i<j} -2J_{ij}\mathbf{S}_i\cdot\mathbf{S}_j \quad (11)$$

where J is the isotropic or Heisenberg exchange coupling constant and $\mathbf{S}_i$ and $\mathbf{S}_j$ are the local spin operators for each metal site. For a system with two metal centers, such as $[2Fe-2S]^{2+}$, this yields a set of levels or "spin ladder" for the total spin S, which ranges from $|S_1 + S_2|$ to $|S_1 - S_2|$. The energies of the total spin states are given by

$$E(S) = -JS(S+1) \quad (12)$$

The isotropic exchange coupling constant J can be thought of as arising from the electrostatic interactions between unpaired electrons localized primarily on one metal center (the "magnetic orbitals") and those localized primarily on the other, and it can be positive (ferromagnetic coupling) or negative (antiferromagnetic coupling).

In mixed-valence systems, such as $[2Fe-2S]^{+}$, the extra electron can reside on either Fe; this doubles the number of total spin states and adds an additional term to the spin Hamiltonian that represents the transfer of the electron from one magnetic orbital to the other, called the double exchange or spin-dependent delocalization term. Accounting for double exchange yields the following equation for the energies of the total spin states

$$E(S) = -JS(S+1) \pm B(S + {}^1/_2) \quad (13)$$

where B is the double exchange term. Because antiferromagnetic isotropic coupling is more commonly encountered (i.e., J is negative), the $|S_1 - S_2|$ state will be the ground state (gs) of the system when $J \gg B$, and conversely, the $|S_1 + S_2|$ state will the gs when $B \gg J$. In the intermediate scenario, all of the intermediate spin states become possible as the gs.

Two additional effects must be considered for mixed-valence systems: static and dynamic asymmetry. Differences in the geometry, hydrogen bonding, and protein electrostatics can cause the extra electron to be localized preferentially on one metal center rather than the other. Although not a factor in symmetric model complexes, such static asymmetry is expected to be very important in proteins. Vibronic coupling, or dynamic asymmetry, arises from the fact that the geometry of the metal center changes when the extra electron migrates from one side to the other. The height of the barrier to electron transfer between the two sides is determined by the magnitude of this distortion. When B is large and the vibronic coupling is small, there is no barrier to intersite electron transfer, and the system is completely *valence-delocalized*. Both static asymmetry and vibronic coupling counteract the effect of double exchange: when these effects are much larger than B, the system is valence-localized. In the case of a localized mixed-valence system, the energies of the total spin states can still be described by eq 13, except that J is replaced by a J_{eff}, which is the regular isotropic exchange coupling constant plus a correction factor to account for double exchange, static asymmetry, and vibronic coupling.

In an exchange-coupled system, the Fermi contact shift for any given total spin state is still described by eq 2. However, the total observed Fermi contact shift is the Boltzmann-weighted average of the isotropic hyperfine coupling constants of each of the total spin states, A_i, which are naturally different. A simple solution to this difficulty lies in the application of the Wigner−Eckart theorem and vector coupling.[34] One can recast the hyperfine coupling constant for each total spin state S in terms of the intrinsic

(30) Gottlieb, H. P. W.; Barfield, M.; Doddrell, D. M. *J. Chem. Phys.* **1977**, *67*, 3785−3794.
(31) Kowalewski, J.; Laaksonen, A.; Nordenskiöld, L.; Blomberg, M. *J. Chem. Phys.* **1981**, *74*, 2927−2930.
(32) Nordenskiöld, L.; Laaksonen, A.; Kowelwski, J. *J. Am. Chem. Soc.* **1982**, *104*.
(33) Kahn, O. *Molecular Magnetism*; Wiley-VCH: New York, 1993.

hyperfine coupling constants for each metal center, A_j. Thus, the observed Fermi contact shift (i.e., the Boltzmann-weighted sum over all total spin states) is[35]

$$\delta_{con} = 10^6\left(\frac{\Delta\nu}{\nu_0}\right)^{con} = -10^6\frac{1}{\hbar\gamma_N B_0}\sum_i\sum_j A_j C_{ji}\langle S_z\rangle_i \quad (14)$$

where C_{ji} represents the spin projection coefficient for each metal center j for each total spin state i. For a binuclear system, C_1 is given by[33−36]

$$C_1 = [S(S+1) + S_1(S_1+1) - S_2(S_2+1)]/[2S(S+1)] \quad (15)$$

in which S is the total spin and S_1 and S_2 are the spin states of the two metal centers. The equation for C_2 is the same, only with the indices reversed. Evaluation of the spin expectation value in eq 14 yields

$$\delta_{con} = 10^6\left(\frac{\Delta\nu}{\nu_0}\right)^{con} = -10^6\frac{g\beta}{\hbar\gamma_N 3kT}\sum_j \frac{A_j\sum_i C_{ji}S(S+1)(2S+1)\exp(-E_S/kT)}{\sum_i (2S+1)\exp(-E_S/kT)} \quad (16)$$

By a similar treatment, one can derive equations for paramagnetic relaxation in exchange-coupled systems as well.[35]

3. Strategy of Directly Detected ^{2}H, ^{13}C, and ^{15}N NMR Spectroscopy

3.1. Why Use Directly Detected ^{2}H, ^{13}C, and ^{15}N NMR Spectroscopy? The largest limitation in paramagnetic NMR spectroscopy is severe line broadening due to paramagnetic relaxation. The nature of the problem differs for different regions of a protein. The resonances of nuclei located a few bonds from the paramagnetic center will be shifted far from typical diamagnetic values and can therefore be observed by simple one-dimensional (1D) NMR experiments. Pulse sequences such as SuperWEFT[37] can be employed that reduce the intensity of the sharp signals from nuclei distant from the metal center ("diamagnetic resonances"), thereby making it easier to identify broad signals. Severe line broadening can still make signals difficult or impossible to observe and can make closely spaced resonances difficult to resolve. A larger problem lies in assigning these broad, hyperfine-shifted resonances. In traditional protein NMR spectroscopy, resonance assignments are accomplished by a suite of two- and three-dimensional (2D and 3D) NMR experiments in which connectivity is established by coherence transfer that occurs via nuclear scalar coupling.[38−40] Rapid nuclear relaxation arising from effects of the paramagnetic center generally precludes such approaches for the broadest, most shifted resonances. An alternative approach relies on detection of a steady-state nuclear Overhauser effect (NOE), which arises indirectly as a result of nuclear−nuclear dipolar coupling.[8] In paramagnetic systems, it is generally assumed that NOEs will be observable only over very short distances, such as geminal protons or protons on the same histidine ring, and therefore can be used for assignment purposes. However, because the NOE is a through-space effect, rather than a through-bond effect, 1D NOEs should be used with caution for assignment purposes (compare, for example, refs 41 and 42). Very fast T_1 relaxation precludes the observation of even steady-state NOEs.

For nuclei that are close to the metal center but are not hyperfine-shifted, the problem is two-fold: while such resonances are still broadened by paramagnetic relaxation, they are overlapped by the intense, sharp diamagnetic signals. Although 2D NMR experiments might permit the resolution of a few such signals, in many cases, paramagnetism renders the entire region up to ∼10 Å around the metal center invisible to traditional multidimensional NMR experiments. Consequently, for years, paramagnetic NMR spectroscopy has been limited to "favorable" systems with fast electronic relaxation in which the paramagnetic line broadening is less severe, such as heme proteins and [4Fe−4S] proteins.

An alternative approach for paramagnetic systems is to dispense with ^{1}H-detected experiments and instead to rely on directly detected ^{2}H, ^{13}C, and ^{15}N 1D and 2D NMR experiments. The three contributions to paramagnetic relaxation (dipolar, Curie, and contact) are each proportional to $1/\gamma_N^2$, where γ_N is the magnetogyric ratio. This means that, in paramagnetic systems, ^{13}C and ^{15}N line widths can be as much as 16- and 100-fold smaller, respectively, than the corresponding ^{1}H line widths. ^{2}H line widths will also be less affected by paramagnetic relaxation; however, facile quadrupolar relaxation can often erase this advantage. In general, directly detected ^{13}C and ^{15}N spectroscopy is rarely performed on proteins, because the signal-to-noise ratio is proportional to $\gamma_N^{5/2}$,[38] yielding 32- and 306-fold lower sensitivity, respectively, compared to ^{1}H NMR spectroscopy. Nonetheless, in the case of severe paramagnetic line broadening, the reduction in line broadening afforded by direct ^{2}H, ^{13}C, and ^{15}N NMR spectroscopy outweighs the lower sensitivity. In addition, the recent introduction of cryogenic probes for the direct detection of ^{13}C can greatly reduce the problem of low sensitivity for this nucleus.[43] 1D ^{2}H, ^{13}C,

(34) Scaringe, R. P.; Hodgson, D. J.; Hatfield, W. E. *Mol. Phys.* **1978**, *35*, 701−713.
(35) Banci, L.; Bertini, I.; Luchinat, C. *Struct. Bonding* **1990**, *72*, 113−136.
(36) Noodleman, L.; Peng, C. Y.; Case, D. A.; Mouesca, J.-M. *Coord. Chem. Rev.* **1995**, *144*, 199−244.
(37) Inubushi, T.; Becker, E. D. *J. Magn. Reson.* **1983**, *51*, 128−133.
(38) Cavanagh, J.; Fairbrother, W. J.; Palmer, A. J.; Skelton, N. J. *Protein NMR Spectroscopy*; Academic Press: New York, 1996.
(39) Wider, G. *BioTechniques* **2000**, *29*, 1278−1294.
(40) Kanelis, V.; Forman-Kay, J. D.; Kay, L. E. *IUMBM Life* **2001**, *52*, 291−302.
(41) Holz, R. C.; Small, F. J.; Ensign, S. A. *Biochemistry* **1997**, *36*, 14690−14696.
(42) Xia, B.; Pikus, J. D.; Xia, W.; McClay, K.; Steffan, R. J.; Chae, Y. K.; Westler, W. M.; Markley, J. L.; Fox, B. G. *Biochemistry* **1999**, *38*, 727−739.
(43) Serber, Z.; Richter, C.; Moskau, D.; Böhlen, J.-M.; Gerfin, T.; Marek, D.; Häberli, M.; Baselgia, L.; Laukien, F.; Stern, A. S.; Hoch, J. C.; Dötsch, V. *J. Am. Chem. Soc.* **2000**, *122*, 3554−3555.

and ^{15}N NMR spectroscopy has been applied in the study of paramagnetic proteins for many years (in the field of iron−sulfur proteins, see, for example, refs 44−46).

3.2. 1D and 2D ^{13}C{X} NMR Spectroscopy. Recently, ^{13}C-detected 2D NMR approaches have permitted connectivity information to be obtained for paramagnetic proteins by scalar coupling-based experiments, even for systems with low electronic relaxation rates. ^{13}C{^{13}C} 2D experiments were originally used for obtaining diamagnetic assignments,[47,48] but were quickly abandoned upon the introduction of ^{1}H-detected 3D methods owing to low sensitivity. Bertini and co-workers used ^{13}C{^{13}C} correlation spectroscopy (COSY) in a study of Ce(III)-substituted calbindin D9k to help assign the ligating carbonyls and used such information in a solution structure determination.[49,50] We developed ^{13}C-{^{13}C} constant-time COSY (CT-COSY) and ^{13}C{^{13}C}-SuperWEFT-CT-COSY as components of a strategy to obtain nearly complete sequential ^{13}C and ^{15}N assignments for paramagnetic proteins with low electronic relaxation rates.[51,52] Pochapsky and co-workers have used ^{13}C{^{13}C} homonuclear multiple quantum spectroscopy (HMQC) to obtain backbone (C′−C$^{\alpha}$) connectivity information.[53]

Sequential assignment depends on obtaining C−N connectivity information; however, this poses a greater challenge than C−C connectivity. Because the one-bond ^{13}C−^{15}N scalar coupling constants ($^{1}J_{CN} \approx 7-15$ Hz) are so much smaller than one-bond ^{13}C−^{13}C scalar coupling constants ($^{1}J_{CC} \approx 35-55$ Hz), pulse sequences require longer delay times to achieve efficient coherence transfer, while rapid T_2 relaxation limits how long delay times can be set before the signal disappears. Nonetheless, Pochapsky and co-workers showed that ^{13}C{^{15}N} heteronuclear multiple quantum correlation spectroscopy (HMQC) could be used to obtain N−C′ connectivities in a paramagnetic protein.[53] An alternative approach is to dispense with 2D NMR methods and rely on 1D heteronuclear difference decoupling.[54] We demonstrated this approach on a [2Fe−2S] ferredoxin labeled selectively with [^{15}N]Cys and [^{13}C′]Ala.[46] Pochapsky and co-workers used extensive selective double labeling and ^{13}C{^{15}N} 1D difference decoupling to obtain backbone assignments for the loops ligating the iron−sulfur cluster in a different [2Fe−2S] ferredoxin.[55−58] We recently showed that selective double labeling is not needed to obtain 1D heteronuclear difference decoupling data and that such spectra are readily obtained, provided the ^{15}N resonances are hyperfine-shifted and therefore can be resolved in a 1D ^{15}N NMR spectrum.[52]

Bertini and co-workers have further developed the use of ^{13}C-detected 2D NMR spectroscopy. They used ^{13}C{^{13}C}-CT-COSY and ^{13}C{^{15}N} heteronuclear single quantum correlation spectroscopy (HSQC) to obtain assignments for the region 6−11 Å from a Cu(II) center with very slow (3 ns) electronic relaxation.[59] They used saturation-recovery ^{13}C-{^{13}C}CT-COSY to obtain ^{13}C T_1 relaxation times in order to obtain distance constraints that were applied in the solution structure determination.[59] Because ^{13}C−^{13}C NOEs become appreciable for larger proteins at sufficiently high magnetic fields,[60] Bertini and co-workers were able to show that one can use directly detected ^{13}C{^{13}C} NOESY to obtain one- and even two-bond connectivities in larger paramagnetic proteins.[61−63]

Currently, there are three basic types of ^{13}C{^{13}C} 2D NMR experiments: CT-COSY, either without[51] or with[52] the SuperWEFT pulse sequence element to remove signals from slowly relaxing diamagnetic resonances; HMQC, either without[53] or with[61] band-selective homonuclear decoupling to remove C′−C$^{\alpha}$ couplings; and NOESY.[61,62] Given the rapid development in this area, more types of ^{13}C{^{13}C} 2D pulse sequences and modifications of these will surely come. Bertini and co-workers have discussed some of the strengths and weaknesses of these experiments.[61,63] In general, the choice of experiment to use will depend on several factors. (1) The first factor is *the type of system.* Bertini and co-workers showed that, for large proteins in which Curie spin relaxation is the dominant contribution to T_2, ^{13}C T_2 values can be short while ^{13}C T_1 values are still quite long for residues near the metal center.[61] In such cases, transfer through the NOE becomes competitive with transfer via scalar couplings, and NOESY is the method of choice. Conversely, for small proteins with low-spin metals center that exhibit slow electronic relaxation, electron−nuclear dipolar relaxation is the dominant contribution to both T_1 and T_2 (except for hyperfine-shifted resonances), making the two comparable, and therefore CT-COSY and HMQC will work better. (2) A second factor is *the type of information desired.* Band-selective homonuclear decoupled HMQC likely offers the best sensitivity and resolution for C′−C$^{\alpha}$

(44) Chan, T.-M.; Markley, J. L. *Biochemistry* **1983**, *22*, 6008−6010.
(45) Cheng, H.; Grohmann, K.; Sweeney, W. *J. Biol. Chem.* **1992**, *267*, 8073−8080.
(46) Cheng, H.; Westler, W. M.; Xia, B.; Oh, B.-H.; Markley, J. L. *Arch. Biochem. Biophys.* **1995**, *316*, 619−634.
(47) Oh, B. H.; Westler, W. M.; Darba, P.; Markley, J. L. *Science* **1988**, *240*, 908−911.
(48) Oh, B.-H.; Mooberry, E. S.; Markley, J. L. *Biochemistry* **1990**, *29*, 4004−4011.
(49) Bertini, I.; Lee, Y.-M.; Luchinat, C.; Piccioli, M.; Poggi, L. *ChemBioChem* **2001**, *2*, 550−558.
(50) Bertini, I.; Donaire, A.; Jiménez, B.; Luchinat, C.; Parigi, G. *J. Biomol. NMR* **2001**, *21*, 85−98.
(51) Machonkin, T. E.; Westler, W. M.; Markley, J. L. *J. Am. Chem. Soc.* **2002**, *124*, 3204−3205.
(52) Machonkin, T. E.; Westler, W. M.; Markley, J. L. *J. Am. Chem. Soc.* **2004**, *126*, 5413−5426.
(53) Kostic, M.; Pochapsky, S. S.; Pochapsky, T. C. *J. Am. Chem. Soc.* **2002**, *124*, 9054−9055.
(54) Weiss, M. A.; Redfield, A. G.; Griffey, R. H. *Proc. Natl. Acad. Sci. U.S.A.* **1986**, *83*, 1325−1329.
(55) Jain, N. U.; Pochapsky, T. C. *J. Am. Chem. Soc.* **1998**, *120*, 12984−12985.
(56) Jain, N. U.; Pochapsky, T. C. *Biochem. Biophys. Res. Commun.* **1999**, *258*, 54−59.
(57) Jain, N. U. Ph.D. Thesis, Brandeis University, Waltham, MA, 2000.
(58) Pochapsky, T. C.; Kostic, M.; Jain, N.; Pejchal, R. *Biochemistry* **2001**, *40*, 5602−5614.
(59) Arnesano, F.; Banci, L.; Bertini, I.; Felli, I. C.; Luchinat, C.; Tompsett, A. R. *J. Am. Chem. Soc.* **2003**, *125*, 7200−7208.
(60) Fischer, M. W. F.; Zeng, L.; Zuiderweg, E. R. P. *J. Am. Chem. Soc.* **1996**, *118*, 12457−12458.
(61) Bermel, W.; Bertini, I.; Felli, I. C.; Kümmerle, R.; Pierattelli, R. *J. Am. Chem. Soc.* **2003**, *125*, 16423−16429.
(62) Bertini, I.; Felli, I. C.; Kümmerle, R.; Moskau, D.; Pierattelli, R. *J. Am. Chem. Soc.* **2004**, *126*, 464−465.
(63) Babini, E.; Bertini, I.; Capozzi, F.; Felli, I. C.; Lelli, M.; Luchinat, C. *J. Am. Chem. Soc.* **2004**, *2004*, 10496−10497.

correlations in many cases, as the signals are all singlets, whereas CT-COSY and NOESY can report on all C−C connectivities. (3) An additional factor is *spectral overlap*. Band-selective homonuclear decoupled HMQC offers superior resolution, whereas SuperWEFT-CT-COSY eliminates all but the most rapidly relaxing signals, allowing one to focus on just these. In principle, the SuperWEFT pulse sequence element could be used in conjunction with nearly any ^{13}C-detected 2D experiment. NOESY with short mixing times offers an alternative method of achieving a similar result.

3.3. Selective Isotopic Labeling. One advantage of 1D and 2D ^{13}C{X} NMR approaches is that they allow assignment information to be obtained on a single uniformly ^{13}C, ^{15}N-labeled protein sample. Methods for uniform isotopic labeling of proteins are well-established and widely applied throughout the field of protein NMR spectroscopy.[64] However, we have found great utility in amino acid selective labeling, in which all amino acid residues in a protein of a particular type (say, cysteine) are isotopically labeled. This allows simple 1D NMR spectroscopy to obtain the immediate assignment to residue type of the broadest hyperfine-shifted signals for which few other methods of assignment are typically available. Although sequential backbone assignments require both N−C′ and C$^{\alpha}$−N connectivities, we have so far been unable to obtain the latter by 1D ^{13}C{^{15}N} difference decoupling. However, a combination of ^{15}N amino-acid-specific labeling and difference decoupling has provided us with sequential backbone assignments.[52] In general, although amino-acid-specific labeling can be used to assign resonances to residue type, other NMR experiments are still required to obtain sequential assignments, some of which might be impossible because of very rapid nuclear relaxation. If a structure is already available, then this information can be used to predict NMR observables, such as relative T_1 relaxation times, or DFT calculations can be performed to calculate hyperfine shifts, which can then be compared to experiment.[65] Alternatively, for sufficiently small proteins, a single amino acid can be isotopically labeled by chemical peptide synthesis followed by protein refolding and metal ion reconstitution. Intein chemistry allows the possibility of isotopically labeling just a portion of a protein,[64,66,67] although, to our knowledge, this approach has yet to be applied to a paramagnetic protein.

The success of amino-acid-specific isotopic labeling depends on the amino acid to be labeled and the type of isotopic label (^{2}H, ^{13}C, or ^{15}N) desired. There are two potential problems associated with amino-acid-specific labeling: (1) low incorporation of the label and (2) scrambling of the label to other amino acid types. The latter is the more serious problem, given that it can lead to ambiguous assignments, whereas the former merely leads to loss of sensitivity. For a more detailed discussion, see ref 68. Although auxotrophic strains are often used to preclude isotopic scrambling, we have found that for many amino acids this is not necessary and that high levels of amino-acid-specific isotopic labeling can be achieved without auxotrophic strains by use of synthetic-rich (SR) media,[46,68] provided one has a highly efficient expression system.[52,69−71] Avoidance of auxotrophic strains allows one to continue to use strains that are highly optimized for protein expression, and SR media help prevent scrambling of the isotopic label by providing *E. coli* with a large excess of the other amino acids.

4. Density Functional Theory Calculations in Paramagnetic NMR Spectroscopy

Until recently, quantum chemical calculations were the realm of theoretical chemists who applied these techniques to molecules with only a few atoms. Calculations of molecules with more than about 10 atoms were limited to those who had access to the most expensive supercomputers of the day. The implementation of density functional theory (DFT), along with the proliferation of user-friendly computer programs, efficient algorithms, and affordable high-speed computers, has enabled the calculation of properties for fairly large molecules (>100 atoms) by nonexperts. DFT generally gives good accuracy for molecular and spectroscopic properties with relatively modest modern computer resources. To obtain approximately the same accuracy as DFT methods, costly second- or higher-order perturbation calculations (MP2, MP4) are necessary. There is a vast literature describing quantum mechanical calculations on molecules.[72−75] Here, we present a tutorial on the practical aspects of applying these calculations for paramagnetic NMR observables.

4.1. Setting up a DFT Calculation. Several commercial and free DFT programs are available. The programs that we use, Gaussian[76] Jaguar,[72,77] and ADF,[73,78] are commercial software packages with well-developed interfaces for input and output. Properties such as the Fermi contact spin density, the spin-differential field gradient tensor (anisotropic hyperfine tensor), and the g tensor can be calculated simply by adding keywords to the input file. The input to a DFT program generally consists of the geometry of the molecule in Cartesian or internal coordinates, the molecular charge, and the multiplicity. Program-specific keywords in the input file drive the calculation. Keyword inputs include the model chemistry method (e.g., B3LYP, PB86, etc.), the basis set (6-311g*, LANL2DZ, etc.), and the desired properties to be computed.

The molecular structures used for DFT calculations must be designed carefully, so that the model is amenable to

(64) Lian, L.-Y.; Middleton, D. A. *Prog. NMR Spectrosc.* **2001**, *39*, 171−190.
(65) Wilkens, S. J.; Xia, B.; Weinhold, F.; Markley, J. L.; Westler, W. M. *J. Am. Chem. Soc.* **1998**, *120*, 4806−4814.
(66) Otomo, T.; Ito, N.; Kyogoku, Y.; Yamazaki, T. *Biochemistry* **1999**, *38*, 16040−16044.
(67) Cowburn, D.; Muir, T. W. *Methods Enzymol.* **2001**, *339*, 41−54.
(68) Muchmore, D. C.; McIntosh, L. P.; Russell, C. B.; Anderson, D. E.; Dahlquist, F. W. *Methods Enzymol.* **1989**, *177*, 44−73.
(69) Chae, Y. K.; Markley, J. L. *Biochemistry* **1995**, *34*, 188−193.
(70) Xia, B. Ph. D. Thesis, University of Wisconsin, Madison, WI, 1997.
(71) Lin, I.-J.; Gebel, E. B.; Machonkin, T. E.; Westler, W. M.; Markley, J. L. *J. Am. Chem. Soc.* **2003**, *125*, 1464−1465.
(72) Friesner, R. A.; Dunietz, B. D. *Acc. Chem. Res.* **2001**, *34*, 351−358.
(73) TeVelde, G.; Bickelhaupt, F. M.; Baerends, E. J.; Fonseca-Guerra, C.; VanGisbergen, S. J. A.; Snijders, J. G.; Ziegler, T. *J. Comput. Chem.* **2001**, *22*, 931−967.
(74) Pople, J. A. *Angew. Chem., Int. Ed.* **1999**, *38*, 1894−1902.
(75) Kohn, W. *Rev. Mod. Phys.* **1999**, *71*, 1253−1266.

calculations with the available technology. To generate a good model, it is necessary to extract the essential details of the structure under study that will produce accurate estimates of properties. This requires some idea of the strengths of various interactions and how they affect the properties being calculated. Generation of the complete structures of small molecules by input of internal coordinates is straightforward, but the de novo construction of an iron−sulfur cluster in a protein is much more difficult. The easiest approach to obtaining the molecular geometry of an active site is to extract coordinates from a Protein Data Bank (PDB) file. To construct active-site structural models from a PDB coordinate file, we select the residues in the immediate vicinity of the iron−sulfur cluster, particularly ligands and hydrogen-bonded residues. To reduce the size of the molecular model, unimportant amino acid side chains can be removed, the caveat being that important delocalization pathways might inadvertently be eliminated. Care must also be taken when removing charged side chains, as this can greatly affect the geometry optimization and the calculated properties. In general, charged side chains are difficult to model, as the charge is often diffuse owing to interactions with other residues in the protein. Often, it is best to remove the charge by adding or removing hydrogen atoms. Empirical partial charges also can be introduced. The C-terminal ends of the peptide are capped with amide or methyl amide groups, and the N-terminal ends are capped with formyl or acetyl groups. Hydrogen atoms must be added if absent from the PDB file. Atoms that are distant from the paramagnetic center can be represented as "ghost atoms", in which a nuclear position is defined in order to calculate relaxation times or psuedocontact shifts, but no electrons are associated with the "atom". This technique is particularly useful for the calculation of T_1 relaxation times of large numbers of atoms, many of which are too distant to experience significant spin delocalization.

Models extracted from high-resolution (∼1-Å) crystal structures work best. Geometry optimization with the positions of the heavy atoms constrained might be required to refine the positions of hydrogen atoms, and optimizations with constrained dihedral angles might be needed to adjust some bond lengths and bond angles. Unconstrained geometry optimization of extracted regions of proteins is usually not effective, as the spatial restrictions afforded by the rest of the protein are absent. The quantum mechanics/molecular mechanics (QMMM) method[79] can be used to optimize the paramagnetic center geometry at the QM level of theory in the presence of the rest of the protein, which is optimized at the MM level of theory. However, if the starting structure is not close to the real structure, then the calculated properties will generally not be accurate.

For the choice of density functionals, we and others have found that the hybrid functional B3LYP gives good accuracy for properties, but that the geometries of iron−sulfur clusters are reproduced more accurately with nonhybrid functionals, such as BP86. Selection of a basis set is also critical. A larger basis set has more flexibility and will typically (but not always) give better results. Many researchers will expand contracted basis sets to better represent the core orbitals or add diffuse functions for better descriptions of longer-range interactions. We typically use the Pople split valence basis (3-21g, 6-31g*, 6-311g**, etc.) but have had success in using effective core potentials on the metal center and split double valence basis on all other atoms (LANL2DZ). In all cases, calibrating the method against experimental results from model compounds is crucial.

4.2. Calculating Paramagnetic NMR Observables. In our experience, the programs Gaussian and ADF are the most flexible in terms of calculating properties relevant to paramagnetic systems. The properties that are available in both of these programs are the isotropic and anisotropic hyperfine couplings, g tensors, spin−orbit coupling energies, and (diamagnetic) chemical shifts. The isotropic couplings yield contact shifts, and the anisotropic couplings (spin-differential field gradient tensor) are used to obtain effective distances in the calculation of T_1 relaxation times. Diamagnetic chemical shift calculations can be used as base values for computing the total chemical shift.

One frustrating part of the calculation of properties is determining the proper factors to use when converting from atomic units, which are used in quantum chemical packages, to SI or other more familiar units. Lists of conversion factors from atomic units to SI units are available from the National Institute of Standards and Technology Web site[80] and from refs 81 and 82.

In Gaussian, a table of isotropic Fermi contact couplings is automatically listed near the end of the output for any unrestricted calculation. In Gaussian 2003, if there are more than 100 atoms in the model, then the keyword "IOp(6/81=1)" is required to print the Fermi contact couplings. In program releases starting with Gaussian 98, the table of Fermi contact couplings is listed in atomic units, megahertz, gauss, and cm^{-1}. The values in atomic units are nucleus-independent and directly comparable.

(76) Frisch, M. J.; Trucks, G. W.; Schlegel, H. B.; Scuseria, G. E.; Robb, M. A.; Cheeseman, J. R.; Montgomery, J. A., Jr.; Vreven, T.; Kudin, K. N.; Burant, J. C.; Millam, J. M.; Iyengar, S. S.; Tomasi, J.; Barone, V.; Mennucci, B.; Cossi, M.; Scalmani, G.; Rega, N.; Petersson, G. A.; Nakatsuji, H.; Hada, H.; Ehara, M.; Toyota, K.; Fukuda, R.; Hasegawa, J.; Ishida, M.; Nakajima, T.; Honda, Y.; Kitao, O.; Nakai, H.; Klene, M.; Li, X.; Knox, J. E.; Hratchian, H. P.; Cross, J. B.; Adamo, C.; Jaramillo, J.; Gomperts, R.; Stratmann, R. E.; Yazayev, O.; Austin, A. J.; Cammi, R.; Pomelli, C.; Ochterski, J. W.; Ayala, P. Y.; Morokuma, K.; Voth, G. A.; Salvador, P.; Dannenberg, J. J.; Zakrzewski, V. G.; Dapprich, S.; Daniels, A. D.; Strain, M. C.; Farkas, O.; Malick, D. K.; Rabuck, A. D.; Raghavachari, K.; Foresman, J. B.; Ortiz, J. V.; Cui, Q.; Baboul, A. G.; Clifford, S.; Cioslowski, J.; Stefanov, B. B.; Liu, G.; Liashenko, A.; Piskorz, P.; Komaromi, I.; Martin, R. L.; Fox, D. J.; Keith, T.; Al-Laham, M. A.; Peng, C. Y.; Nanayakkara, A.; Challacombe, M.; Gill, P. M. W.; Johnson, B.; Chen, W.; Wong, M. W.; Gonzalez, C.; Pople, J. A. *Gaussian 03*, revision A.1; Gaussian, Inc.: Pittsburgh, PA, 2003.
(77) See www.schrodinger.com (accessed Jan 12, 2005).
(78) Fonseca-Guerra, C.; Snijders, J. G.; TeVelde, G.; Baerends, E. J. *Theor. Chim. Acta* **1998**, *99*, 391.
(79) Monard, G.; Merz, K. M. *Acc. Chem. Res.* **1999**, *32*, 904−911.
(80) *The NIST Reference on Constants, Units, and Uncertainty*; National Institute of Standards and Technology (NIST): Gaithersburg, MD, 2002; see physics.nist.gov/constants (accessed Jan 12, 2005).
(81) Mohr, P. J.; Taylor, B. N. *Rev. Mod. Phys.* **2000**, *72*, 351−495.
(82) Mohr, P. J.; Taylor, B. N. *J. Phys. Chem. Ref. Data* **1999**, *28*, 1713−1852.

When calculating effective distances for use in the Solomon−Bloembergen−Morgan equation (eq 7), the spin-differential field gradient tensor is required. In Gaussian 03, this can be obtained with the keyword "prop=EPR", and in versions prior to Gaussian 03, it can be obtained with the keyword "prop=EFG IOp(6/17=1,6/26=4)". The table entitled "Anisotropic Spin Dipole Couplings in Principal Axis System" has the eigenvalues listed as Baa, Bbb, and Bcc. These values are first divided by the number of unpaired spins and then multiplied by 6.748725×10^{30} to convert from bohr^{-3} to meters^{-3} (note that bohr is a unit of length). This yields the values of $\langle q_{xx}\rangle_{spin}$, $\langle q_{yy}\rangle_{spin}$, and $\langle q_{zz}\rangle_{spin}$, respectively (the off-diagonal elements being 0), that can be used in eq 8 to calculate r_{eff}.

In antiferromagnetic dimers, the exchange coupling between the metal atoms complicates the computation of properties. As described in section 2.3, two centers that have spins S_1 and S_2 can be combined to give a coupled representation with values from $|S_1 - S_2|$ to $|S_1 + S_2|$. The energies of the successive spin states are given by eq 12. Direct calculation of the coupled spin states requires a multideterminantal wave function, which is difficult to formulate and computationally expensive. An approach developed by Noodleman for investigating coupled spin systems is to calculate a broken-symmetry state, which is an averaged antiferromagnetic state, and a high-spin ferromagnetic state, which can be represented by a single-determinantal wave function.[36] We have developed an approach that uses Clebsch−Gordon coefficients and spin projection to rework the unpaired spin density in the broken-symmetry state into intrinsic values for each metal center. This is derived in the Supporting Information. With this approach, the intrinsic metal center hyperfine couplings can be obtained by solving a pair of simultaneous equations.

Our method requires convergence to a high-spin state, which is usually facile, and convergence to the broken-symmetry state, which is not. Convergence to the broken-symmetry state is hampered by the absence of a good initial guess. Noodleman solved this problem for ADF by obtaining a converged wave function for the high-spin state and then modifying the wave function to resemble the broken-symmetry state and converging to self-consistency. The modification consists of swapping the α and β spins on one of the metal atoms. Recently, Morales and Weinhold developed an approach, Natural Guess, based on natural bond orbital theory, in which an initial guess for the broken-symmetry state can be obtained from the converged high-spin state.[83]

In our hands, calculation of the broken-symmetry state has been successful for small models of the active site of oxidized [2Fe−2S] clusters,[84] but not for larger models that incorporate hydrogen bonds and therefore would give more accurate calculated properties, because of the lack of a good initial guess and therefore lack of convergence. A much simpler alternative approach for obtaining the intrinsic Fermi contact coupling constants for the individual atoms in [2Fe−2S] clusters is to perform a pair of calculations in which a diamagnetic metal ion is substituted for each of the iron atoms. We use Ga^{3+} as a substitute for Fe^{3+} and Zn^{2+} as a substitute for Fe^{2+}. The intrinsic couplings are combined by using the spin-projection coefficients to obtain the property for the full cluster. This technique is described in more detail in sections 5.3 and 5.4.

5. Applications to Iron−Sulfur Proteins

5.1. Rubredoxin. Rubredoxin, the simplest iron−sulfur protein, contains a single Fe ligated by four cysteines. The availability of high-resolution X-ray structures makes it an excellent model system for paramagnetic NMR studies. In *Clostridium pasteurianum* rubredoxin (CpRd), the hyperfine-shifted ^{1}H resonances are extremely broad (up to ∼80 kHz), and those arising from the Cys H^β protons are not observable in the oxidized state. However, the 1D ^{2}H, ^{13}C, and ^{15}N NMR spectra of both redox states exhibit numerous sharp, well-resolved hyperfine-shifted signals. The ^{2}H, ^{13}C, and ^{15}N resonances of the ligating cysteines were identified in both oxidation states by the use of selective ^{2}H, ^{13}C, and ^{15}N labeling, including the incorporation of chirally deuterated cysteine and single-site labeling by chemical peptide synthesis (Figures 1 and 2, Table S1).[70,85−88] The ^{15}N spectra showed, in addition to the four hyperfine-shifted resonances of the ligating cysteines, eight additional hyperfine ^{15}N resonances (Figure 2). These have been assigned by amino-acid-specific labeling[70,86,87] and confirmed by single-site labeling and ^{13}C{^{13}C} and ^{13}C{^{15}N} NMR experiments.[88]

Three crystal structures of oxidized CpRd at 1.1−1.2-Å reslution are available.[89−91] From each of these, a 104-atom model was constructed. DFT calculations were performed on these models to calculate several different NMR observables.[65,92]/

DFT calculations of the Fermi contact shifts yielded excellent agreement (Figure 3) with the experimental ^{2}H and ^{15}N hyperfine shifts for all three models (in one, a correction to the placement of the amide protons was required). The calculations helped to confirm assignments in cases for which single-site labeling had not yet been achieved. Note that, for hs Fe(III), the pseudocontact shift is small enough that it can safely be ignored. The level of agreement is perhaps

(83) Weinhold, F. Department of Chemistry, University of Wisconsin, Madison, WI. Personal communication, 2004.

(84) Westler, W. M.; Markley, J. L. Department of Biochemistry and Nuclear Magnetic Resonance Facility at Madison, University of Wisconsin, Madison, WI. Unpublished results, 2004.
(85) Xia, B.; Westler, W. M.; Cheng, H.; Meyer, J.; Moulis, J.-M.; Markley, J. L. *J. Am. Chem. Soc.* **1995**, *117*, 5347−5350.
(86) King, D. S. University of California, Berkely, CA. Xia, B.; Volkman, B. F.; Jenk, D.; LeMaster, D. M.; Westler, W. M.; Wilkens, S. J.; Markley, J. L. University of Wisconsin, Madison, WI. Unpublished data, 1997.
(87) Xia, B.; Wilkens, S. J.; Westler, W. W.; Markley, J. L. *J. Am. Chem. Soc.* **1998**, *120*, 4893−4894.
(88) Lin, J.; Machonkin, T. E.; Westler, W. M.; Markley, J. L. University of Wisconsin, Madison, WI. Unpublished data, 2004.
(89) Watenpaugh, K. D.; Sieker, L. C.; Jensen, L. H. *J. Mol. Biol.* **1979**, *131*, 509−522.
(90) Watenpaugh, K. D.; Sieker, L. C.; Jensen, L. H. *J. Mol. Biol.* **1980**, *138*, 615−633.
(91) Dauter, Z.; Wilson, K. S.; Sieker, L. C.; Moulis, J. M.; Meyer, J. *Proc. Natl. Acad. Sci. U.S.A.* **1996**, *93*, 8836−8840.
(92) Wilkens, S. J.; Xia, B.; Volkman, B. F.; Weinhold, F.; Markley, J. L.; Westler, W. M. *J. Phys. Chem. B* **1998**, *102*, 8500−8505.

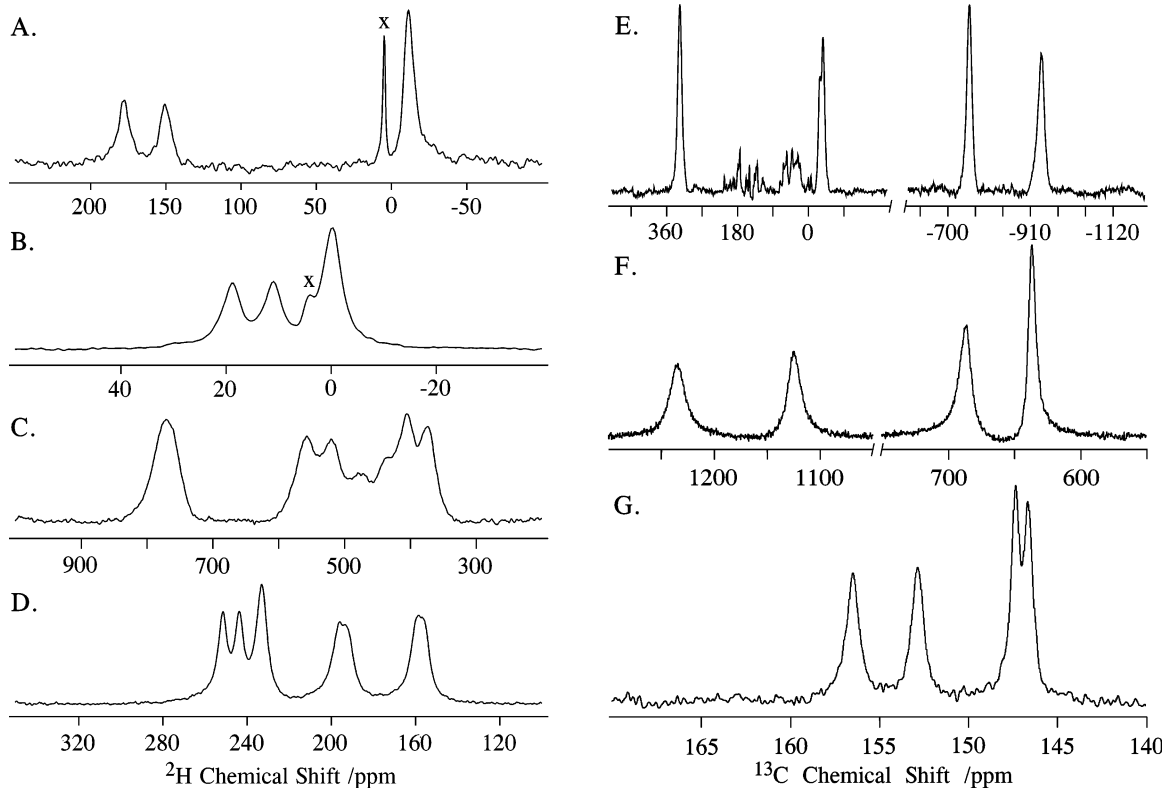

Figure 1. NMR spectra of ^{2}H- and ^{13}C-labeled *Clostridium pasteurianum* rubredoxin. (A) ^{2}H NMR spectrum of oxidized [^{2}H$^\alpha$]Cys-labeled CpRd. The peak labeled × arises from ^{1}H^{2}HO. (B) ^{2}H NMR spectrum of reduced [^{2}H$^\alpha$]Cys-labeled CpRd. The peak labeled x arises from ^{1}H^{2}HO. (C) ^{2}H NMR spectrum of oxidized [^{2}H$^\beta$]Cys-labeled CpRd. (D) ^{2}H NMR spectrum of reduced [^{2}H$^\beta$]Cys-labeled CpRd. (E) ^{13}C NMR spectrum of reduced [^{13}C$^\beta$]Cys-labeled CpRd. (F) ^{13}C NMR spectrum of reduced [U−^{13}C]-labeled CpRd, showing the Cys C$^\alpha$ resonances. (G) ^{13}C NMR spectrum of reduced [^{13}C′]Cys-labeled CpRd. Parts A−D adapted from ref 85. Part E adapted from ref 9.

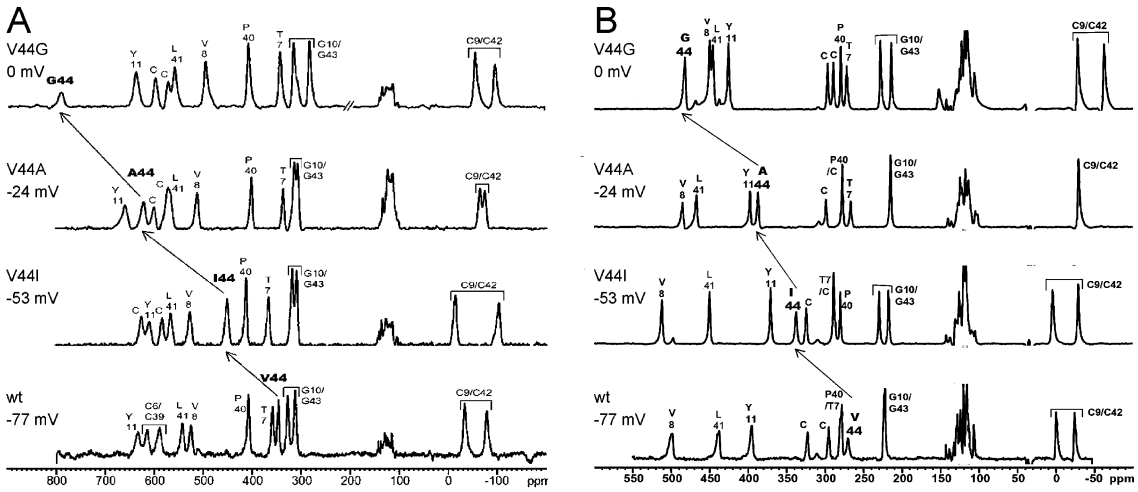

Figure 2. 1D ^{15}N NMR spectra of the wild type and V44I, V44A, and V44G mutants of *Clostridium pasteurianum* rubredoxin in the (A) oxidized and (B) reduced states. The reduction potentials as reported by Wedd and co-workers are listed at the left.[105] Assignments are given above each peak. The ^{15}N resonance of position 44 and how it changes in each variant is highlighted. Part A is reproduced with permission from ref 71. Copyright 2003 American Chemical Society.

surprising, given the well-known limitations of DFT in calculating open-shell transition metal systems, and especially given that the magnitudes of the unpaired spin densities calculated for these Fermi contact shifts are so small. We suspect, however, that this counterintuitive phenomenon is widespread among transition metal systems; indeed, similarly excellent agreement between experiment and theory has been obtained for the hyperfine couplings in blue copper proteins.[93]

A second surprising result was that the large hyperfine shifts observed for the eight ^{15}N resonances that were not from the ligating cysteines were strongly influenced by hydrogen bonding. CpRd contains six backbone amides that donate H-bonds to Cys S$^\gamma$ atoms: Val8, Cys9, Tyr11, Leu41, Cys42, and Val44 (Figure 4A). In particular, the amide nitrogens of Tyr11 and Val44 exhibit large hyperfine shifts but are eight covalent bonds from the Fe. This demonstrates that hydrogen bonds are capable of delocalizing electron spin

(93) Jaszewski, A. R.; Jezierska, J. *Chem. Phys. Lett.* **2001**, *343*, 571−580.

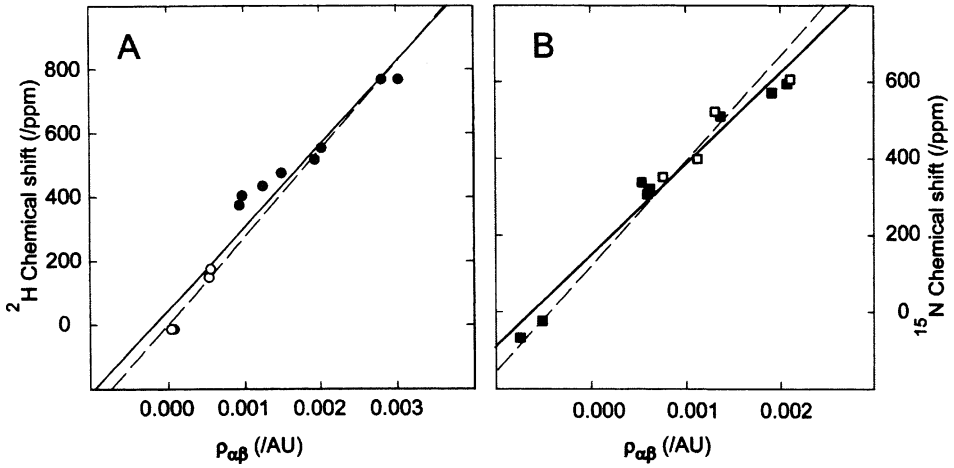

Figure 3. Linear regression fits of the experimental (A) ^{2}H and (B) ^{15}N chemical shifts of oxidized *Clostridium pasteurianum* rubredoxin versus the unpaired spin density ($\rho_{\alpha\beta}$) calculated as described in the text. The solid lines correspond to the best fits to the data, and the dashed lines indicate the theoretical correlation. Reproduced with permission from ref 65. Copyright 1998 American Chemical Society.

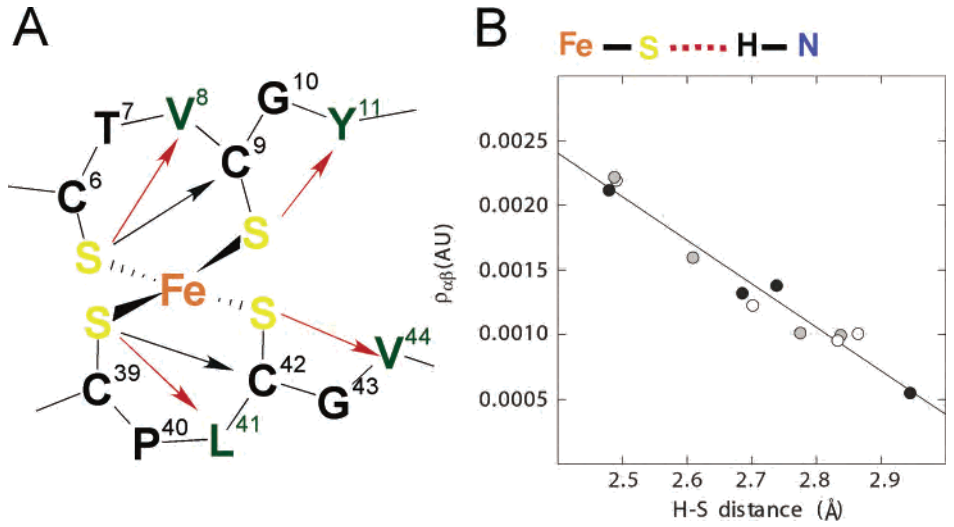

Figure 4. (A) Schematic representation of the active site of *Clostridium pasteurianum* rubredoxin, with the hydrogen bonds to the cysteine S$^\gamma$'s represented as arrows. (B) Correlation between the calculated unpaired spin density ($\rho_{\alpha\beta}$) at the amide nitrogens of residues V8, Y11, L41, and V44 for the structural models derived from the three different crystal structures (white, gray, and black circles) and the H···S hydrogen bond distances in those structures. Reproduced with permission from ref 65. Copyright 1998 American Chemical Society.

density, yielding substantial ^{15}N Fermi contact shifts. Furthermore, the calculations showed a strong correlation between the magnitude of the hyperfine shift and the H···S$^\gamma$ distance (Figure 4B). Note that the ^{15}N resonances of the cysteine ligands must be considered separately, because they also derive appreciable unpaired spin density through covalent bonds. The delocalization of unpaired spin density onto hydrogen-bonding amide nitrogens is confirmed by the fact that these resonances show a large (≥8 ppm) ^{1}H/^{2}H isotope effect (Table S1, in parentheses), which again is accounted for quantitatively by DFT calculations.[87] These results showing the ability of NH···S$^\gamma$ to transmit Fermi contact shifts are similar to results obtained earlier on Cd-substituted Rd, which showed nuclear scalar couplings between the hydrogen-bonded amide protons and the ^{113}Cd, thus demonstrating for the first time the ability of hydrogen bonds to transmit scalar couplings.[94]

DFT calculations have also been performed on reduced CpRd. Initially, no crystal structure of reduced CpRd was available, so calculations were performed on the oxidized structure with the redox state of the metal changed to Fe(II).[65] Despite the obvious weakness of this approach, good agreement was obtained between the calculated and observed ^{2}H and ^{13}C resonances, which, in fact, provided some of the specific assignment in cases where single-site labeling was not available. Much poorer agreement was found for the ^{15}N resonances, likely indicating small structural differences in the hydrogen bonds of the oxidized and reduced proteins (Figure 5A). Recently, a 1.2-Å resolution crystal structure of reduced CpRd became available.[95] DFT calculations of models constructed from this structure show an improved correlation between experimental and calculated hyperfine shifts (Figure 5B); however, the correlation is still not nearly as good as that obtained for the oxidized protein.[84] This could be due to the lower resolution of the crystal structure, or it might indicate that the structure of reduced CpRd is subtly

(94) Blake, P. R.; Park, J. B.; Adams, M. W. W.; Summers, M. F. *J. Am. Chem. Soc.* **1992**, *114*, 4931−4933.
(95) Min, T.; Ergenekan, C. E.; Eidsness, M. K.; Ichiye, T.; Kang, C. *Protein Sci.* **2001**, *10*, 613−621.

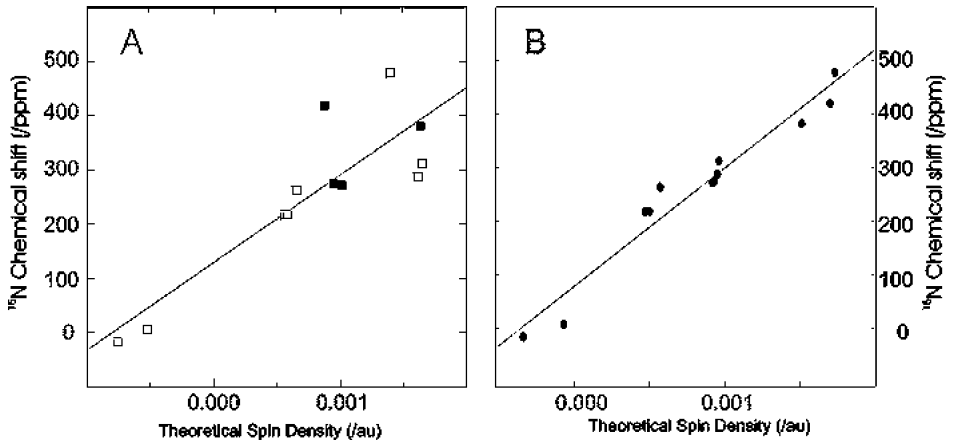

Figure 5. Linear regression fits of the experimental ^{15}N chemical shifts of reduced *Clostridium pasteurianum* rubredoxin versus the unpaired spin density ($\rho_{\alpha\beta}$). The solid lines correspond to the best fits to the data, and the dashed lines indicate the theoretical correlation. (A) Results calculated from a structural model derived from one of the crystal structures of oxidized CpRd (4RXN).[89,90] (B) Results calculated from a structural model derived from the crystal structure of reduced CpRd (1FHM).[95] Part A is reproduced with permission from ref 65. Copyright 1998 American Chemical Society.

different in solution. Ongoing experimental and computational studies hopefully will yield insight into this issue.

The fact that the ^{15}N hyperfine shifts in this simple iron−sulfur protein are inversely related to the H···S$^{\gamma}$ distance allows paramagnetic ^{15}N NMR spectroscopy to be used as a very precise "molecular ruler" for a series of mutants of CpRd: a change in H···S$^{\gamma}$ distance of just 0.1 Å (which is at or below the limit of precision for a ∼1.0-Å crystal structure) will yield a change in the ^{15}N hyperfine shift of 89 ppm. The factors that tune the redox potentials of metalloproteins have been of long-standing interest (see, for example, refs 96−101); these include the possible role of hydrogen bonding to the active site. More than 25 different single- and double-site mutants of CpRd have been constructed, with redox potentials spanning a range of >150 mV.[102−105] In the crystal structure, two of the residues that contribute hydrogen bonds to the ligating cysteines, V8 and V44, are situated with their isopropyl side chains on the surface, and most of the van der Waals contacts of these side chains are with each other rather than with other parts of the protein.[105] Mutations at one of these two sites to residues with side chains of different size, such as isoleucine, alanine, or glycine, can modulate the length of just one hydrogen bond with minimal perturbation to the rest of the structure, as was confirmed by crystallography for the V44A and V44I mutants.[105] Mutations of V44 lead to a systematic increase in the reduction potential from the wild-type value of −77 mV to the V44G mutant with a value of 0 mV. The ^{15}N NMR spectra convincingly demonstrate that decreasing the length of this particular NH···S$^{\gamma}$ bond by ∼0.5 Å leads to this increased redox potential.[71] An excellent correlation was found between the reduction potential and the ^{15}N hyperfine shift in the oxidized state (Figure 6). A similar trend is seen in the reduced state.[88] Further work is needed to fully define the nature of the hydrogen-bond differences between the oxidized and reduced states and the exact mechanism whereby these hydrogen bonds preferentially stabilize the reduced state.

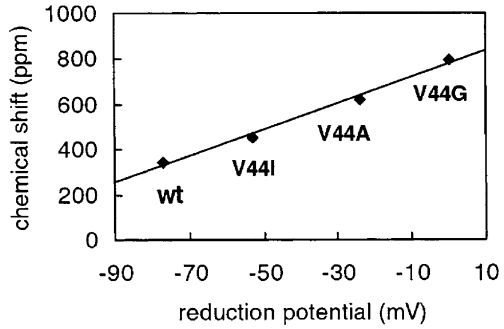

Figure 6. Plot of the ^{15}N chemical shifts of the amide nitrogen at position 44 for the wild type and V44I, V44A, and V44G mutants of oxidized *Clostridium pasteurianum* rubredoxin versus the reduction potential. Reproduced with permission from ref 71. Copyright 2003 American Chemical Society.

DFT calculations were also used to a obtain a quantitative understanding of the ^{15}N T_1 relaxation rates in oxidized CpRd.[92] As discussed above, the paramagnetic contributions to the T_1 times are dominated by electron−nuclear dipolar relaxation. However, it was shown that the point-dipole approximation is a poor model for ^{15}N nuclei <7 Å from the Fe(III) center. This is not surprising given that there is appreciable covalency in the Fe−S bond,[106] which would lead to a large ligand-centered contribution. As discussed in section 2.2, DFT allows one to calculate elements of the spin-differential field gradient tensor and, in turn, an "effective

(96) Stephens, P. J.; Jollie, D. R.; Warshel, A. *Chem. Rev.* **1996**, *96*, 2491−2513.
(97) Bertini, I.; Gori-Savellini, G.; Luchinat, C. *J. Biol. Inorg. Chem.* **1997**, *2*, 114−118.
(98) Mauk, G.; Moore, G. R. *J. Biol. Inorg. Chem.* **1997**, *2*, 119−125.
(99) Gunner, M. R.; Alexov, E.; Torres, E.; Lipovaca, S. *J. Biol. Inorg. Chem.* **1997**, *2*, 126−134.
(100) Warshel, A.; Papazyan, A.; Muegge, I. *J. Biol. Inorg. Chem.* **1997**, *2*, 143−152.
(101) Capozzi, F.; Ciurli, S.; Luchinat, C. *Struct. Bonding* **1998**, *90*, 127−160.
(102) Ayhan, M.; Xiao, Z.; Lavery, M. J.; Hamer, A. M.; Nugent, K. W.; Scrofani, S. D. B.; Guss, M.; Wedd, A. G. *Inorg. Chem.* **1996**, *35*, 5902−5911.
(103) Kümmerle, R.; Zhuang-Jackson, H.; Gaillard, J.; Moulis, J.-M. *Biochemistry* **1997**, *36*, 15983−15991.
(104) Eidsness, M. K.; Burden, A. E.; Richie, K. A.; Kurtz, D. M.; Scott, R. A.; Smith, E. T.; Ichiye, T.; Beard, B.; Min, T.; Kang, C. *Biochemistry* **1999**, *38*, 14803−14809.
(105) Xiao, Z.; Maher, M. J.; Cross, M.; Bond, C. S.; Guss, J. M.; Wedd, A. G. *J. Biol. Inorg. Chem.* **2000**, *5*, 75−84.

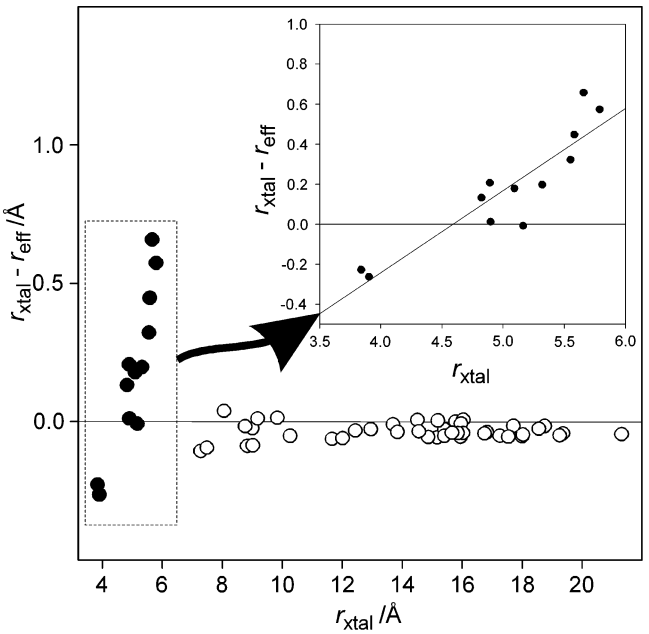

Figure 7. Plot of $r_{xtal} - r_{eff}$ versus r_{xtal}, where r_{xtal} is the measured distance between individual ^{15}N nuclei and the Fe atom in the 4RXN crystal structure[89,90] and r_{eff} is the effective distance calculated from the wave function using the spin-differential field gradient tensor method. Black circles represent ^{15}N nuclei that give rise to hyperfine-shifted resonances, and open circles represent the "diamagnetic" ^{15}N nuclei. The horizontal line is drawn at the zero of the abscissa. The inset plot shows an expansion of the ordinate for nuclei that are close to the metal center. Reproduced with permission from ref 92. Copyright 1998 American Chemical Society.

distance", r_{eff}, that quantitatively accounts for unpaired spin delocalization. The use of r_{eff} provided excellent agreement between experimental ^{15}N T_1 times and those calculated with the Solomon−Bloembergen−Morgan equation (eq 7) for nuclei close to the Fe(III) center (Figure 7). The only adjustable parameter is τ_c, which was found to be $\sim 4 \times 10^{-10}$ s. In this system, $\tau_c \approx \tau_e$, and this value is typical for Fe^{3+}.

5.2. Identification and Classification of ^{1}H and ^{13}C Hyperfine-Shifted Resonances in Different [2Fe−2S] Ferredoxins. Ferredoxins (Fd's) can be classified broadly into three types: plant-type, vertebrate-type, and clostridial-type, based in part on sequence homology.[107,108] X-ray crystal structures have been determined for representative members of the plant (*Anabaena*)[109] and vertebrate types (bovine)[110] in the oxidized state, in which the two exhibit essentially identical metrical parameters for the [2Fe−2S] cluster.

In contrast, in the reduced state, the plant- and vertebrate-type Fd's exhibit electronic structures that are highly conserved within each class but dramatically different between classes.[111−114] Reduced plant-type Fd's exhibit rhombic EPR spectra (*g* values: 2.05, 1.96, 1.88) and effective isotropic exchange coupling constants (J_{eff}) of −75 to −115. Vertebrate-type Fd's have axial EPR spectra (*g* values: 2.02, 1.94, 1.94) and much stronger antiferromagnetic coupling ($J_{eff} \approx -250$). Bertrand and co-workers derived a ligand-field model that explained the electronic structure differences between the reduced plant-type and hydroxylase-type *g*, ^{57}Fe hyperfine, and electric-field gradient tensors in terms of a C_{2v} distortion of the Fe^{II} ion that mixes $d_{x^2-y^2}$ character into the mostly d_{z^2} ground state.[111,113] Systematic differences are also seen in the reduction potential of plant- and vertebrate-type ferredoxins: −433 to −345[115−123] and −295 to −230 mV,[124] respectively. Last, vertebrate-type Fd's exhibit a conformational change upon reduction, an unusual feature for an electron-transfer protein, as shown definitively for human Fd by our NMR chemical shift data.[125] The lack of high-quality structures of reduced Fd's have precluded a detailed understanding of these interesting differences.

We have compared the paramagnetic NMR spectra of representative members of the plant and vertebrate Fd's: *Anabaena* PCC7210 and human Fd, respectively. The assignment of the resonances are discussed below, and more detailed analyses are presented in sections 5.4 and 5.5. The paramagnetic NMR spectra of the oxidized states of the two proteins are very similar. The ^{1}H hyperfine-shifted resonances are extremely broad and unresolved, but the ^{13}C hyperfine-shifted resonances are quite well resolved. The Cys H^{β}, H^{α}, C^{β}, C^{α}, and C′ resonances have been assigned to residue and atom type by selective ^{2}H and ^{13}C labeling in oxidized human Fd[52,126,127] and in oxidized *Anabaena* Fd[46,127,128] Cys C′−C^{α} connectivities were obtained by ^{13}C{^{13}C} CT-COSY in human Fd[51] and *Anabaena* Fd[128] Cys H^{α}−C^{α} connectivities in human Fd were obtained by 1D ^{1}H{^{13}C} difference decoupling[52] but were not seen in *Anabaena* Fd.[128] These

(106) Rose, K.; Shadle, S. E.; Eidness, M. K.; Kurtz, D. M.; Scott, R. A.; Hedman, B.; Hodgson, K. O.; Solomon, E. I. *J. Am. Chem. Soc.* **1998**, *120*, 10743−10747.
(107) Bertini, I.; Luchinat, C.; Provenzani, A.; Rosato, A.; Vasos, P. R. *Proteins: Struct. Funct. Genet.* **2002**, *46*, 110−127.
(108) Meyer, J. *FEBS Lett.* **2001**, *509*, 1−5.
(109) Morales, R.; Chron, M.-H.; Hudry-Clergeon, G.; Pétillot, Y.; Norager, S.; Medina, M.; Frey, M. *Biochemistry* **1999**, *38*, 15764−15773.
(110) Müller, A.; Müller, J. J.; Muller, Y. A.; Uhlmann, H.; Berhardt, R.; Heinemann, U. *Structure* **1998**, *6*, 269−280.
(111) Bertrand, P.; Gayda, J.-P. *Biochim. Biophys. Acta* **1979**, *579*, 107−121.
(112) Sands, R. H.; Dunham, W. R. *Q. Rev. Biophys.* **1975**, *7*, 443−504.
(113) Guigliarelli, B.; Bertrand, P. *Adv. Inorg. Chem.* **1999**, *47*, 421−497.
(114) Fu, W.; Drozdzewski, P. M.; Davies, M. D.; Sligar, S. G.; Johnson, M. K. *J. Biol. Chem.* **1992**, *267*, 15502−15510.
(115) Holden, H. M.; Jacobson, B. L.; Hurley, J. K.; Tollin, G.; Oh, B.-H.; Skjeldahl, L.; Chae, Y. K.; Cheng, H.; Xia, B.; Markley, J. L. *J. Bioenerg. Biomembr.* **1994**, *26*, 67−88.
(116) Fee, J. A.; Palmer, G. *Biochim. Biophys. Acta* **1971**, *245*, 175−195.
(117) Fee, J. A.; Mayhew, S. G.; Palmer, G. *Biochim. Biophys. Acta* **1971**, *245*, 196−200.
(118) Cammack, R.; Rao, K. K.; Bargeron, C. P. *Biochem. J.* **1977**, *168*, 205−209.
(119) Bottin, H.; Lagoutte, B. *Biochim. Biophys. Acta* **1992**, *1101*, 48−56.
(120) Gayda, J.-P.; Gibson, J. F.; Cammack, R.; Hall, D. O. *Biochim. Biophys. Acta* **1976**, *434*, 154−163.
(121) Andrew, P. W.; Rogers, L. J.; Boulter, D.; Haslett, B. G. *Eur. J. Biochem.* **1976**, *69*, 243−248.
(122) Kerscher, L.; Oesterhelt, D.; Cammack, R.; Hall, D. O. *Eur. J. Biochem.* **1976**, *71*, 101−107.
(123) Werber, M. M.; Mevarech, M. *Arch. Biochem. Biophys.* **1978**, *187*, 447−456.
(124) Lambeth, J. D.; McCaslin, D. R.; Kamin, H. *J. Biol. Chem.* **1976**, *251*, 7545−7550.
(125) Xia, B.; Volkman, B. F.; Markley, J. L. *Biochemistry* **1998**, *37*, 3965−3973.
(126) Skjeldahl, L.; Markley, J. L.; Coghlan, V. M.; Vickery, L. E. *Biochemistry* **1991**, *30*, 9078−9083.
(127) Xia, B.; Jenks, D.; LeMaster, D. M.; Westler, W. M.; Markley, J. L. *Arch. Biochem. Biophys.* **2000**, *373*, 328−334.
(128) Machonkin, T. E.; Westler, W. M.; Markley, J. L., manuscript in preparation.

data are listed in Table S2. Sequential cysteine assignments are still lacking for both proteins.

In the plant-type Fd's, the hyperfine resonances are far narrower in the reduced state than in the oxidized state, thus facilitating their assignment. In reduced *Anabaena* PCC7120 vegetative Fd, extensive assignments were obtained for the Cys H^{β}, H^{α}, C^{β}, and N resonances through selective labeling, 2D NOESY (tailored for fast-relaxing resonances), 2D ^{1}H-{^{13}C} HSQC, 1D heteronuclear decoupling, and ^{13}C{^{13}C} CT-COSY experiments (Table S3).[46,127−129] Very similar ^{1}H hyperfine data have been obtained for other plant-type Fd's.[130]

In contrast to the plant-type Fd's, the NMR spectra of vertebrate-type Fd's display much larger line widths in the reduced form than in the oxidized. This indicates that, whereas the electronic relaxation rates of oxidized plant- and vertebrate-type Fd's are essentially the same, in the reduced state, vertebrate-type Fd's have much lower electronic relaxation rates than plant-type Fd's, possibly even lower than Fd's in the oxidized state. This makes resonance assignments difficult. We have assigned the Cys H^{β}, H^{α}, C^{β}, C^{α}, and C′ resonances residue and atom type by selective ^{2}H and ^{13}C labeling.[127,128] Reduced [2Fe−2S] Fd's are assumed to be valence-trapped, with the extra electron localized on a specific Fe center (vide infra). On the basis of the theoretical model of hyperfine shifts described below, one can readily predict a qualitative pattern of which cysteine resonances will be shifted upfield and which downfield of the diamagnetic values. This allows us to narrow down the assignments to the pair of cysteines ligating the Fe(III), Cys92 and 55, and the pair ligating the Fe(II), Cys 46 and 41. These data are summarized in Table S3.

5.3. Implementation of a Strategy for Paramagnetic Resonance Assignments Based on ^{13}C and ^{15}N NMR Spectroscopy: Oxidized Human Ferredoxin, a Case Study. We have used oxidized human Fd as a model system for developing our novel strategy for obtaining nearly complete resonance assignments for paramagnetic proteins with low electronic relaxation rates.[52] The assignment strategy consists of six steps. First, the diamagnetic region of the protein is assigned by use of standard ^{1}H-detected 2D and 3D NMR methods. Second, the broadest, hyperfine-shifted ^{1}H and ^{13}C resonances, namely, those arising from the ligands, are assigned to residue and atom type by selective isotopic labeling and 1D NMR spectroscopy, as discussed above. Third, ^{13}C{^{13}C} 2D NMR experiments such as CT-COSY are used to identify the spin systems from the remaining residues that are within ∼10 Å of the paramagnetic center and therefore cannot be identified by traditional ^{1}H-detected NMR spectroscopy. Fourth, the ^{15}N resonances of these residues are identified by residue type through selective ^{15}N labeling and 1D ^{15}N NMR. Fifth, 1D ^{13}C{^{15}N} difference decoupling is used to establish sequential connectivities and assignments resulting from prior identifications of C′ and N signals by residue type. Last, once the ^{13}C resonance assignments are available, one can extend these to ^{1}H assignments by properly optimized ^{1}H-detected experiments; however, we have found that the number of new ^{1}H assignments obtained by this approach is small compared to the effort involved.

Figure 8 shows several regions of the paramagnetic-optimized ^{13}C{^{13}C} CT-COSY spectrum of [U−^{13}C, ^{15}N]-labeled oxidized human Fd, primarily those regions that contain C^{α}−C^{β} cross-peaks. Most of the cross-peaks could be identified immediately on the basis of previously obtained diamagnetic ^{13}C resonance assignments. The relatively small number of remaining cross-peaks, which are highlighted with black ovals, are therefore identified as belonging to residues near the paramagnetic center that were not observed in the traditional ^{1}H-detected NMR experiments. In the case of this protein, these cross-peaks experience very little pseudocontact shift, so they can be tentatively assigned to residue type on the basis of patterns of ^{13}C chemical shifts and, in many cases, further connectivities along the carbon side chain that uniquely identify the spin system. A few remaining ^{13}C resonances could be assigned to amino acid type by process of elimination. By this method, at least part of the ^{13}C spin system for every residue in the [2Fe−2S] cluster binding loops could be identified.

The C′−C^{α} correlations that are required for sequence-specific assignments could not be obtained from the same ^{13}C{^{13}C} CT-COSY spectrum owing to severe spectral overlap. This problem was solved by developing a pulse sequence that places a SuperWEFT element in front of the ^{13}C{^{13}C} CT-COSY component in order to suppress the slowly relaxing diamagnetic resonances and permit the resolution and identification of just the desired rapidly relaxing signals. As seen in Figure 9, the only cross-peaks remaining are those belonging to the residues in the cluster binding loops.

A number of ^{15}N resonances were assigned to residue type by selective ^{15}N labeling of threonine, glycine, leucine, alanine, and cysteine. Because so many of the ^{15}N resonances were hyperfine-shifted and therefore clearly resolved in a 1D spectrum, C′−N correlations were obtained on [U−^{13}C, ^{15}N]-labeled protein by difference decoupling (see Figure 10). With the C′ and N resonances identified by amino acid type, sequence-specific assignments were obtained readily for all but A45 and A51, which could not be differentiated because the protein sequence contains two Ala-Cys dipeptides.

Application of a few paramagnetic ^{1}H-detected 2D and 3D experiments provided a few additional ^{1}H assignments. Overall, extensive sequence-specific backbone and side-chain ^{13}C and ^{15}N assignments were obtained for essentially all of the residues in the cluster binding loops, with the exception of the cysteine ligands, whose signals were assigned by residue type but not by residue number. These results are summarized in Table 2 of ref 52.

5.4. DFT Calculations of ^{1}H and ^{13}C Hyperfine Shifts in Oxidized [2Fe−2S] Ferredoxins: Validation of the Method. We have implemented DFT calculations of ^{1}H and

(129) Skjeldahl, L.; Westler, W. M.; Oh, B.-H.; Krezel, A. M.; Holden, H. M.; Jacobson, B. L.; Rayment, I.; Markley, J. L. *Biochemistry* **1991**, *30*, 7363−7368.
(130) Dugad, L. B.; La Mar, G. N.; Banci, L.; Bertini, I. *Biochemistry* **1990**, *29*, 2263−2271.

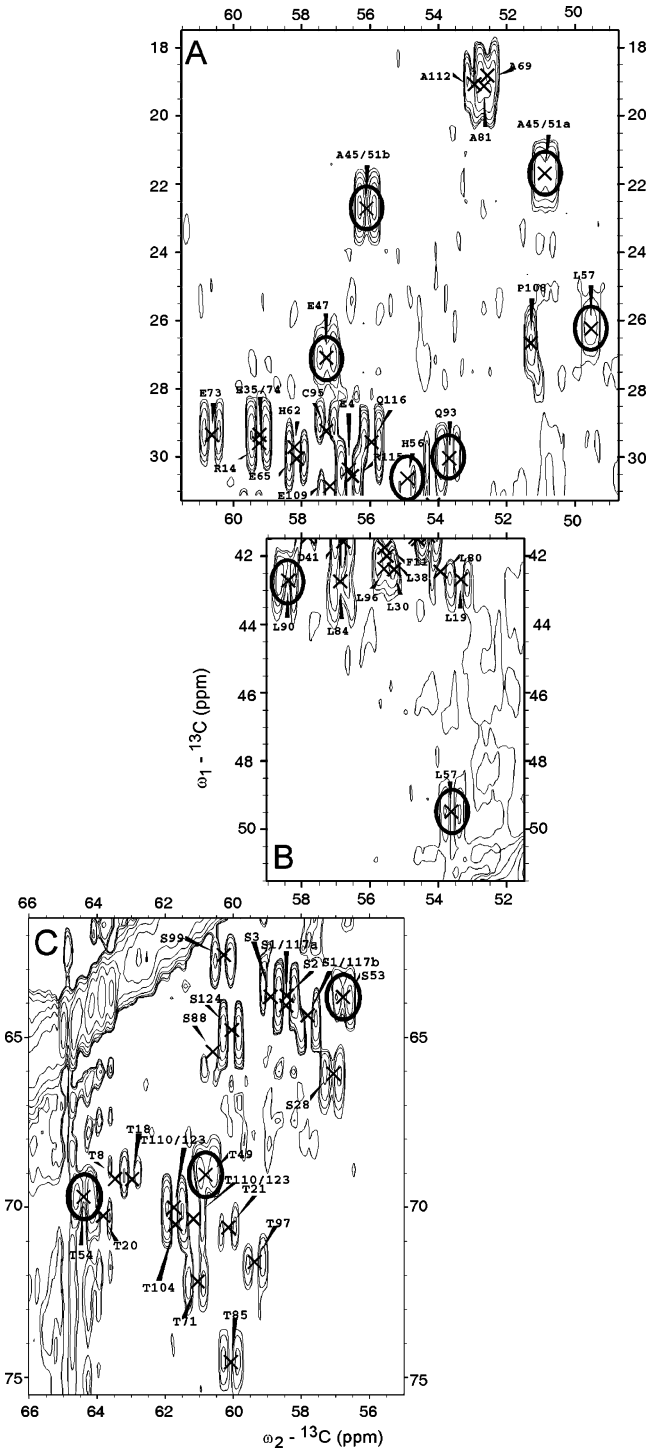

Figure 8. $^{13}C\{^{13}C\}$ CT-COSY spectrum of [U−^{13}C, ^{15}N]-labeled oxidized human Fd ($HuFd_{ox}$) acquired with parameters optimized for rapidly relaxing signals. (A) contains primarily $C^{\alpha}-C^{\beta}$ cross-peaks of Ala, Glu, Gln, and His residues, (B) contains primarily $C^{\alpha}-C^{\beta}$ cross-peaks of Leu residues, and (C) contains $C^{\alpha}-C^{\beta}$ cross-peaks of Ser and Thr residues. Spectra are phased such that, in the direct dimension, diagonal peaks are in-phase absorptive, and cross-peaks are antiphase dispersive. Connectivities that were not observed in traditional ^{1}H-detected 3D spectra are highlighted with black ovals. Adapted from ref 52.

^{13}C hyperfine shifts in human and *Anabaena* Fd's, based on models constructed from the 1.85-Å crystal structure of oxidized bovine (a close homologue to the human) Fd[110] and the 1.3-Å crystal structure of oxidized *Anabaena* Fd's.[109]

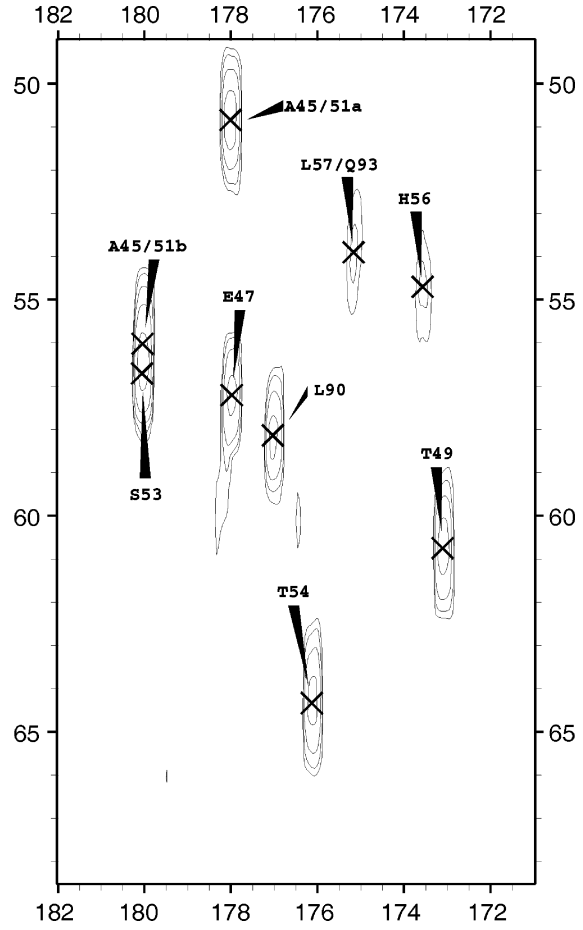

Figure 9. $^{13}C\{^{13}C\}$ SuperWEFT-CT-COSY spectrum of [U−^{13}C, ^{15}N]-$HuFd_{ox}$. The region shown contains the backbone $C'-C^{\alpha}$ cross-peaks. Adapted from ref 52.

Details of this work will be presented in a forthcoming paper; here, we present key insights obtained from this study.

First, DFT calculations were performed on oxidized human and *Anabaena* Fd. Because the crystal structures are for the oxidized proteins, the only significant modification needed was the addition of protons. From this, three different models were constructed for each protein. The first model consists of the [2Fe−2S] cluster with the four cysteines modeled as ethanethiolates but with no other changes to the crystallographic coordinates (the "EtS^{-}" model). The second model is the same as the first, only with the hydrogen bonds to the cysteine S^{γ}'s and the bridging sulfides modeled as hydrogen fluoride molecules placed at the same position as the HN or HO moieties in the crystal structures and with OH moieties added to the ethanethiolates in the positions corresponding to the cysteine amides (the "EtS^{-} + HF" model). The third model consists of the [2Fe−2S] cluster with the four cysteine ligands and the entire cluster binding loop peptides (the "peptide" model). For each of these three models of the two protein active sites, two calculations were performed. In the first, metal center 1 (M_1) in the [2Fe−2S] cluster, which is ligated by Cys41 and 46 in *Anabaena* Fd and by Cys46 and 53 in human Fd, was an Fe(III), and metal center 2 (M_2), which is ligated by Cys49 and 79 in *Anabaena* Fd and by Cys55 and 92 in human Fd, was a Ga(III). In the second calculation, the Fe(III) and Ga(III) were interchanged. Fermi

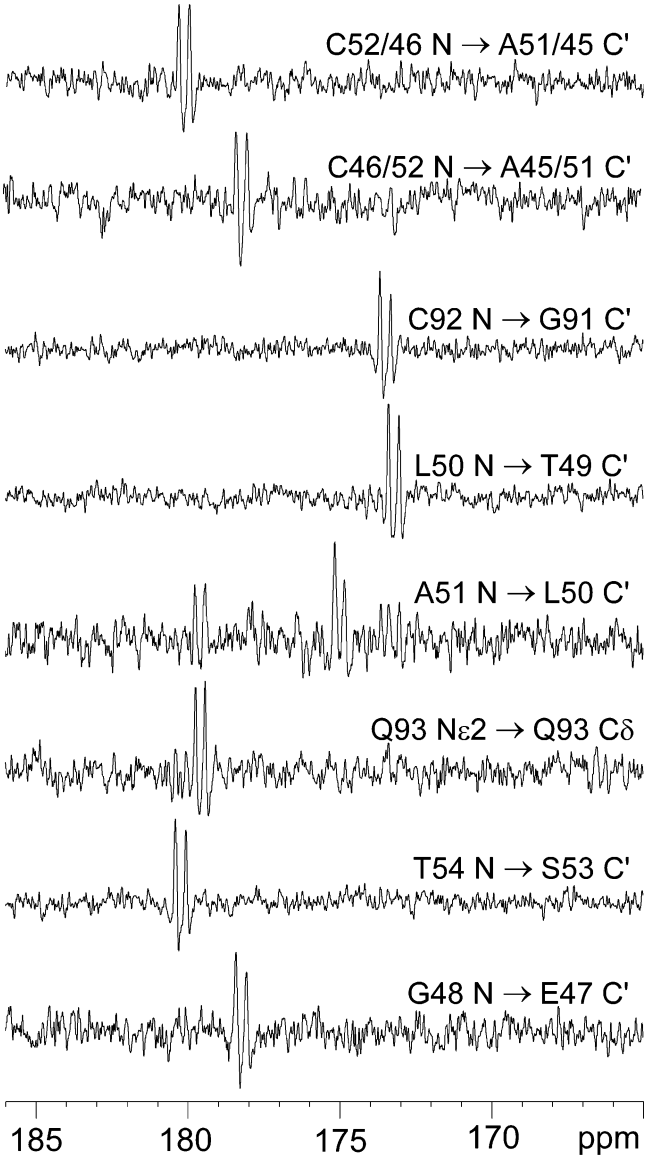

Figure 10. 1D $^{13}C\{^{15}N\}$ difference decoupling NMR spectra of [U−^{13}C, ^{15}N]-HuFd$_{ox}$. The spectra are labeled according to the ^{15}N signal that was selectively decoupled and the corresponding ^{13}C carbonyl resonance that was identified. Reproduced with permission from ref 52. Copyright 2004 American Chemical Society.

contact shifts were calculated as per the procedure outlined in sections 2.3 and 4.2. The experimentally determined value of -175 cm^{-1} for the isotropic exchange coupling was used. The similarity of the hyperfine shifts in these two oxidized Fd's justifies the use of the same value for the exchange coupling. To these Fermi contact shifts were added the average diamagnetic chemical shifts for cysteine resonances, as obtained from the BMRB (BioMagResBank),[131] for comparison of calculated and experimental chemical shifts (Figure 11).

One key result of this study is the importance of hydrogen bonding in determining the cysteine ^1H and ^{13}C hyperfine shifts. Without the inclusion of any hydrogen bonds to the sulfurs, very poor correlation was observed between calculated and experimental hyperfine shifts. This is most noticeable for the ^{13}C resonances, which are clearly resolved: even the signs of the cysteine C^β hyperfine shifts are not correctly predicted in the EtS^- model. Modeling of the hydrogen bonds to the cysteine S^γ's as HF (for the cysteine amides, as OH) dramatically improves the correlation between calculated and experimental hyperfine shifts for both the ^1H and ^{13}C resonances, despite the obvious crudeness of this model for a hydrogen-bonding amide. Additional, but much smaller changes are seen in the calculated values for the peptide model. Indeed, the peptide model is not clearly superior to the EtS^- + HF model, which likely reflects the limited accuracy of the crystal structures from which these models were derived.

5.5. DFT Calculations of ^1H and ^{13}C Hyperfine Shifts in Reduced [2Fe−2S] Ferredoxins: Insights into the Degree of Valence Trapping. The success of the calculation of hyperfine shifts in oxidized [2Fe−2S] proteins prompted us to consider such a study for the reduced proteins. In the reduced [2Fe−2S] Fd's, the sign, magnitude, and temperature dependence of the cysteine ligand ^1H hyperfine shifts have been treated by a theoretical model developed by Dunham[132] and later extended by Banci and Bertini.[35,133] This vector coupling approach to understanding hyperfine shifts was presented in section 2.3. The key equation is eq 21, and one very important underlying assumption in its use for the calculation of hyperfine shifts for mixed-valence systems is that the extra electron is "trapped", *i.e., entirely localized on one Fe center*. Given this equation, assuming that the intrinsic hyperfine coupling constants for cysteine H^β and H^α protons are 1.0 and 0.1 MHz, respectively; assuming that these nuclei are coupled only to the closer of the two Fe centers; and allowing the value of J_{eff} to float, then one can obtain good agreement with the experimental hyperfine data on plant-type Fd's. However, the value of J_{eff} obtained from this procedure is only about one-half the experimentally determined value of -100 cm^{-1} for plant-type Fd's[112,120,134−137] Nonetheless, the conclusion from the application of this model for the hyperfine shifts of reduced plant-type Fd's is that this system is indeed valence-trapped, even at room temperature on the NMR time scale, and that the extra electron resides entirely on the Fe ligated to Cys 41 and 46 (M_1).[35,130] The same conclusion is reached for the vertebrate Fd's, namely, that the system is valence-trapped and that M_1 (ligated by Cys46 and 53) is the Fe(II) center. The J_{eff} value obtained from this procedure is much more negative than that in plant-type Fd's, which is the correct trend, but again it is only about one-half of the experimental value of -250 cm^{-1}.

(131) BioMagResBank, Department of Biochemistry, University of Wisconsin, Madison, WI, www.bmrb.wisc.edu (accessed Jan 12, 2005).
(132) Dunham, W. R.; Palmer, G.; Sands, R. H.; Bearden, A. J. *Biochim. Biophys. Acta* **1971**, *253*, 373−384.
(133) Bertini, I.; Ciurli, S.; Luchinat, C. *Struct. Bonding* **1995**, *83*, 1−53.
(134) Palmer, G.; Dunham, W. R.; Fee, J. A.; Sands, R. H.; Iikuka, T.; Yonetani, T. *Biochim. Biophys. Acta* **1971**, *245*, 201−207.
(135) Anderson, R. E.; Dunham, W. R.; Sands, R. H.; Bearden, A. J.; Crespi, H. L. *Biochim. Biophys. Acta* **1975**, *408*, 306−318.
(136) Lloyd, S. G.; Franco, R.; Moura, J. J. G.; Moura, I.; Ferreira, G. C.; Huynh, B. H. *J. Am. Chem. Soc.* **1996**, *118*, 9892−9900.
(137) Salerno, J. C.; Ohnishi, T.; Blum, H.; Leigh, J. S. *Biochim. Biophys. Acta* **1977**, *494*, 191−197.

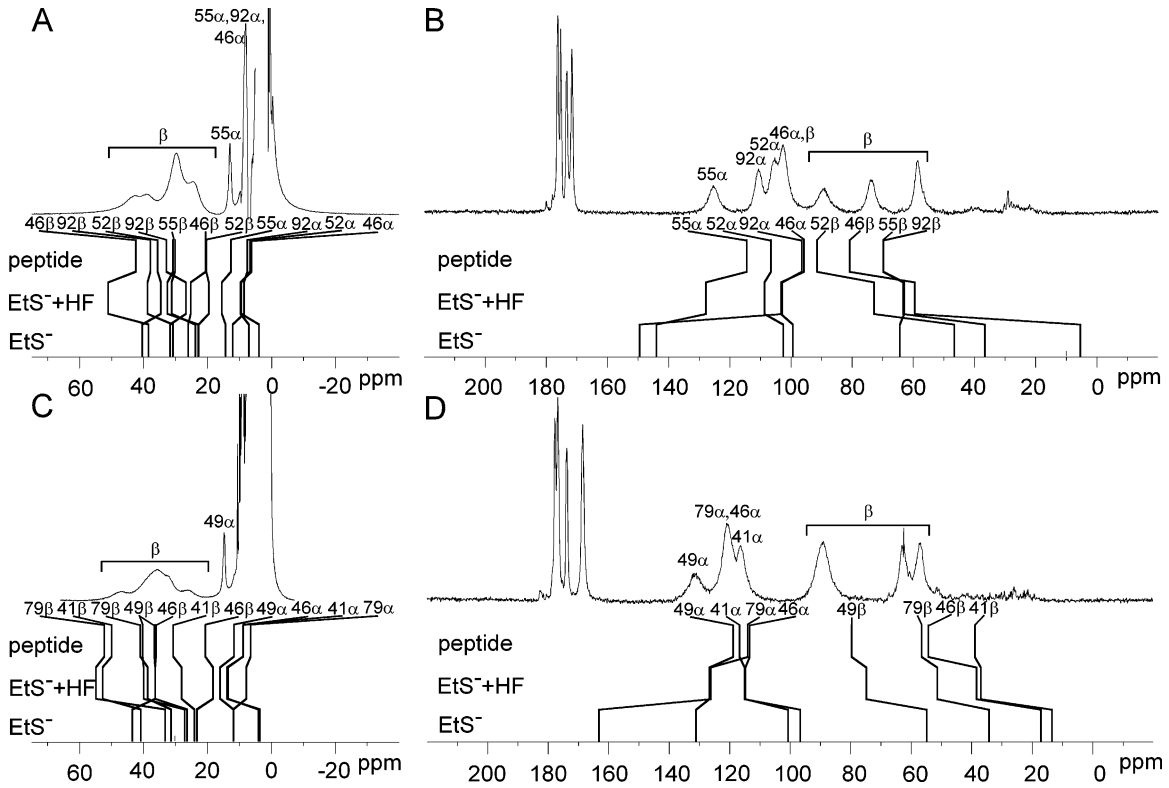

Figure 11. Comparison of the 1D ^{1}H and ^{13}C NMR spectra of oxidized human and *Anabaena* Fd's with the calculated chemical shifts for the three models (peptide, EtS^- + HF, and EtS^-) as described in the text. The calculated chemical shifts for each model are indicated with vertical lines. Diagonal lines connect these to show how these calculated chemical shifts change for each of the models. The best possible assignments of the experimental data are given above each peak. Definitive assignments are available only to atom type; the residue-specific assignments given here are based on comparison to calculated hyperfine and T_1 relaxation data and are therefore tentative. (A) ^{1}H NMR spectrum of unlabeled human Fd. (B) ^{13}C NMR spectrum of [U−^{13}C]Cys-labeled human Fd. (C) ^{1}H NMR spectrum of unlabeled *Anabaena* Fd. (D) ^{13}C NMR spectrum of [U−^{13}C]Cys-labeled *Anabaena* Fd.

For the calculation of hyperfine shifts in reduced human and *Anabaena* Fd's, we relied on the same oxidized crystal structures as above for construction of the models, as reliable structures of reduced [2Fe−2S] Fd's are currently unavailable. For each protein, two calculations were performed. In the first, M_1 was Fe(II), because that was the result of the semiquantitative analyses of the hyperfine shifts outlined above, and M_2 was Ga(III). In the second calculation, M_1 was Zn(II), and M_2 was Fe(III). For the reduced metal center, either Fe(II) or Zn(II), the M_1-S^γ and M_1−sulfide bond distances were increased by 0.05 and 0.1 Å, respectively. Only the EtS^- + HF model was used, and the XH···S hydrogen bond distances and angles were kept the same as in the oxidized crystal structures. The reasons for this were that (1) the calculations on the oxidized state demonstrated that hydrogen bonding must be taken into account in order to yield reasonable agreement with experimental data, but that the results of the EtS^- + HF model and the full peptide model were not greatly different, and (2) whereas we could fix the XH···S distances and angles without altering other aspects of the structure in the EtS^- + HF model, this was not possible in the full peptide model. Although the XH···S distances and angles surely change upon reduction, we do not currently have any way of determining how these change, and geometry optimization of these models is beyond the scope of present capabilities. Hyperfine shifts were calculated as per sections 2.3 and 4.2. We used the experimentally determined J_{eff} values for plant- and vertebrate-type Fd's (−100 and −250 cm^{-1}, respectively).

The experimental ^{1}H and ^{13}C hyperfine data for reduced human and *Anabaena* Fd were compared with results from this calculation (labeled "100/0"). The agreement (Figure 12A and B) is very good for reduced human Fd. The correct trends are observed for the ^{1}H and ^{13}C hyperfine shifts for all four cysteine ligands, and in most cases, the computationally derived values are close to where ^{1}H and ^{13}C resonances are experimentally observed. The agreement is much poorer for reduced *Anabaena* Fd (Figure 12C and D). The calculated values do *not* exhibit the correct trends: the hyperfine shifts of the Cys49 and Cys79 H^β's and C^α's are much too large, and the hyperfine shifts of the Cys41 and Cys46 H^β's, H^α's, and C^α's are of the wrong sign. There is no reason to ascribe this result to poor accuracy of the crystallographically derived structural model, given that (1) the crystal structure of oxidized *Anabaena* Fd was at higher resolution, (2) the agreement between calculated and experimental hyperfine shifts was equally good for oxidized *Anabaena* and human Fd, and (3) *Anabaena* Fd is not believed to undergo any significant structural change upon reduction. One source of the discrepancy between the calculated and experimental hyperfine shifts is the value used for J_{eff}. Any error in J_{eff} as experimentally determined from magnetic susceptibility or temperature-dependent EPR data will have a large impact on the calculated values of the

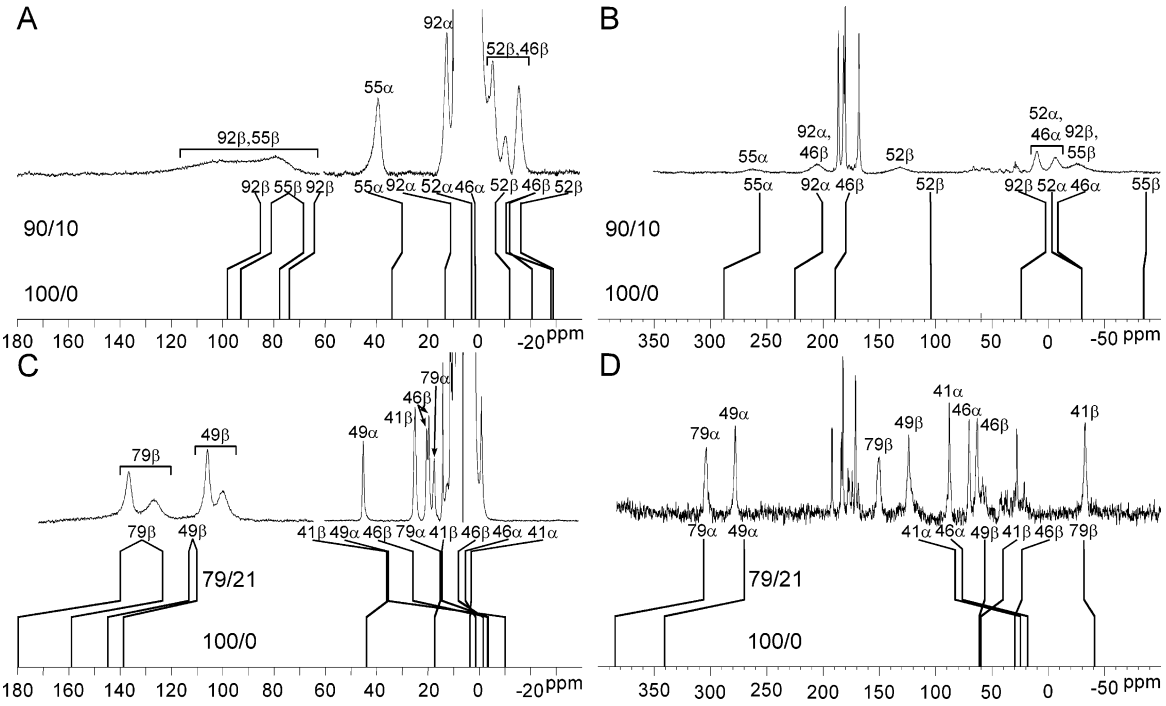

Figure 12. Comparison of the 1D ^{1}H and ^{13}C NMR spectra of reduced human and *Anabaena* Fd's with the calculated chemical shifts for the $EtS^- + HF$ model. The calculated chemical shifts are indicated with vertical lines. Two different sets of calculated chemical shifts are given. The first is assuming that the system is entirely valence-trapped, i.e., M_1/M_2 is purely Fe(II)/Fe(III). This is denoted 100/0. The second is assuming that the system is a time-averaged mixture of a major form in which M_1/M_2 is Fe(III)/Fe(II) and a minor form in which M_1/M_2 is Fe(III)/Fe(II). These calculated chemical shifts are denoted by the percentages of the major and minor forms: 90/10 for human Fd and 79/21 for *Anabaena* Fd. The best possible assignments of the experimental data are given above each peak. For *Anabaena* Fd, these assignments are definitive and were obtained by a variety of experimental approaches described in the text. For human Fd, definitive assignments are available only to atom type; the residue-specific assignments given here are based on comparison to the calculated hyperfine shifts and are therefore tentative. (A) ^{1}H NMR spectrum of unlabeled human Fd. (B) ^{13}C NMR spectrum of [U−^{13}C]Cys-labeled human Fd. (C) ^{1}H NMR spectrum of unlabeled *Anabaena* Fd. (D) ^{13}C NMR spectrum of [U−^{13}C]Cys-labeled *Anabaena* Fd.

hyperfine shifts. However, adjustment of J_{eff} cannot improve the agreement between the calculated and experimental values. Making J_{eff} more negative will decrease the hyperfine shifts of the Cys49 and Cys79 H^{β}'s and C^{α}'s to bring them into agreement with experiment, but will make the hyperfine shifts of the Cys41 and Cys46 H^{β}'s, H^{α}'s and C^{α}'s even more negative. Making J_{eff} less negative will make the hyperfine shifts of the Cys41 and Cys46 H^{β}'s, H^{α}'s and C^{α}'s positive and therefore in agreement with experiment, but will make the hyperfine shifts of the Cys49 and Cys79 H^{β}'s and C^{α}'s far too large. An alternative explanation is needed.

Another potential source of the discrepancy between the calculated and experimental hyperfine shifts is the assumption of complete valence trapping. The assumption of a dynamically delocalized model in which the major form has M_1 as Fe(II) and M_2 as Fe(III) and the minor form has M_1 as Fe(III) and M_2 as Fe(II) will decrease the hyperfine shifts of the Cys49 and 79 and will make the hyperfine shifts of the Cys41 and 46 weakly positive rather than weakly negative. This was accomplished by performing a second pair of calculations in which M_1/M_2 was Fe(III)/Zn(II) and then Ga(III)/Fe(II). A linear combination of the result of the first set of calculations with that of this second set, which made the implicit assumption that the rate of intervalence charge-transfer is fast on the NMR time scale, yielded final calculated hyperfine shifts that again were compared with the experimental data (Figure 12C and D). For reduced human Fd, inclusion of 10% of the minor form, in which M_1/M_2 is Fe(III)/Fe(II), improved the correlation between calculated and experimental values for some resonances but not others. Larger amounts of the minor form led to a rapid deterioration in the level of agreement. For reduced *Anabaena* Fd, inclusion of 21% of the minor form yielded the best correlation between calculated and experimental values, which was considerably improved over the purely valence-trapped calculation.

This demonstrates that, in the case of reduced vertebrate-type Fd's, the assumption of valence trapping is well-founded. The extra electron is indeed localized on the M_1 center, within the level of accuracy offered by our calculations. For reduced plant-type Fd's, our data indicate that partial delocalization yields a minor species in which the extra electron is on the M_2 center. The analysis of the different factors that could cause J to be the same between plant- and vertebrate-type Fd's in the oxidized state but J_{eff} to differ by a factor of 2.5 in the reduced state is clearly beyond the scope of this paper. However, the results presented here demonstrate that the large difference in static asymmetry must be taken into account. This difference in the level of valence trapping might also contribute to the systematic difference in the redox potentials of plant- and vertebrate-type Fd's. Finally, these results demonstrate the ability of paramagnetic NMR spectroscopy and DFT calculations to provide insights into the room-temperature electronic structures of metal centers that cannot be obtained by any other means.

6. Concluding Remarks

Because of complications resulting from interactions between unpaired spin density at a paramagnetic center and nearby nuclei, methods developed for diamagnetic proteins are not applicable to what usually is the most interesting part of the molecule. Thus, NMR investigations of paramagnetic proteins (or other macromolecules) require new methods and approaches. As discussed here, a combined approach that involves the optimization of NMR experiments, the production of selectively labeled proteins, and the application of DFT calculations provides a powerful means for probing the geometric and electronic structures of paramagnetic centers in proteins. We have presented results in this Forum article describing our work on the iron−sulfur clusters in rubredoxin and in [2Fe−2S] ferredoxins. Labeling strategies and paramagnetic relaxation optimized NMR pulse sequences have led to the assignment of resonances corresponding to most of the nuclei that are strongly affected by electron−nuclear dipolar relaxation. The experimental contact shifts and relaxation parameters are faithfully reproduced with DFT calculations on models derived from high-resolution crystal structures. The combination of experiment and theory provides structural constraints for nuclei near the iron−sulfur clusters, which will permit the structural refinement of the most important region in paramagnetic proteins. The NMR and associated computational techniques are beginning to provide information about the presence and strengths of hydrogen bonds and their effect on the structure and redox characteristics of iron−sulfur clusters.

As these techniques are refined and advanced, we foresee the extension of these methods to other paramagnetic systems. We are currently investigating methods for further optimization of pulse sequences, measurement of residual dipolar coupling constants (to be used as further constraints in the structural refinement), and separation and measurement of contact and pseudocontact shifts.

Acknowledgment. Support by NIH Grants RR02301 (which provides partial support to the National Magnetic Resonance Facility at Madison) and GM58667 is gratefully acknowledged. We thank the several students and postdocs cited here who have made important contributions to this work.

Supporting Information Available: Derivation of intrinsic unpaired spin densities for each metal center in a coupled system from the broken-symmetry and high-spin states that can be calculated from DFT. Experimental chemical shifts and assignments of the hyperfine-shifted resonances in oxidized and reduced *Clostridium pasterianum* rubredoxin (Table S1), oxidized human and *Anabaen*a PCC7120 ferredoxins (Table S2), and reduced human and *Anabaen*a PCC7120 ferredoxins (Table S3). This material is available free of charge via the Internet at http://pubs.acs.org.

IC048624J